

PREDICTION OF COKE FORMATION OVER A CATALYST PARTICLE FOR DRY REFORMING
OF METHANE



Miss Chananun Rojanarungruengporn

จุฬาลงกรณ์มหาวิทยาลัย
CHULALONGKORN UNIVERSITY

A Thesis Submitted in Partial Fulfillment of the Requirements
for the Degree of Master of Engineering in Chemical Engineering

Department of Chemical Engineering

FACULTY OF ENGINEERING

Chulalongkorn University

Academic Year 2021

Copyright of Chulalongkorn University

การทำนายการเกิดโค้งบนอนุภาคของตัวเร่งปฏิกิริยาสำหรับปฏิกิริยาอีพอกซ์-อิมิดะแบบแห้งของมีเทน



วิทยานิพนธ์นี้เป็นส่วนหนึ่งของการศึกษาตามหลักสูตรปริญญาวิศวกรรมศาสตรมหาบัณฑิต

สาขาวิชาวิศวกรรมเคมี ภาควิชาวิศวกรรมเคมี

คณะวิศวกรรมศาสตร์ จุฬาลงกรณ์มหาวิทยาลัย

ปีการศึกษา 2564

ลิขสิทธิ์ของจุฬาลงกรณ์มหาวิทยาลัย

ชานันท์ โรจนรุ่งเรืองพร : การทำนายการเกิดโค้กบนอนุภาคของตัวเร่งปฏิกิริยาสำหรับ
 ปฏิกิริยารีฟอร์มมิงแบบแห้งของมีเทน. (PREDICTION OF COKE FORMATION OVER
 A CATALYST PARTICLE FOR DRY REFORMING OF METHANE) อ.ที่ปรึกษาหลัก :
 ผศ. ดร.สุพจน์ พัฒนะศรี, อ.ที่ปรึกษาร่วม : ดร.ศุภฤกษ์ ประเสริฐธรรม,ดร.พทธี
 ประเสริฐเจริญสุข,ดร.กริชชาติ ว่องไวลิขิต

ในปัจจุบันภาวะโลกร้อนเป็นปัญหาทางสิ่งแวดล้อมที่สำคัญซึ่งส่งผลกระทบต่อทั่วโลก ปฏิกิริยารีฟอร์มมิงแบบแห้งของมีเทน เป็นหนึ่งในปฏิกิริยาที่สามารถใช้คาร์บอนไดออกไซด์ได้อย่างมีประสิทธิภาพ อย่างไรก็ตามปัญหาหลักของกระบวนการรีฟอร์มมิงแบบแห้งของมีเทน คือการเสื่อมสภาพของตัวเร่งปฏิกิริยาซึ่งเกิดจากการก่อตัวของโค้กบนตัวเร่งปฏิกิริยา ซึ่งส่วนใหญ่เกิดขึ้นจากปฏิกิริยาการสลายตัวของมีเทน การก่อตัวของโค้กทำให้ประสิทธิภาพของตัวเร่งปฏิกิริยาลดลงโดยการอุดตันรูพรุน และส่วนที่ว่องไวบนตัวเร่งปฏิกิริยา ในงานวิจัยนี้ได้ตรวจสอบการเสื่อมสภาพของตัวเร่งปฏิกิริยาที่เกิดจากการก่อตัวของโค้กบนตัวเร่งปฏิกิริยานิกเกิลบนตัวรองรับอลูมินาทรงกลมในปฏิกิริยารีฟอร์มมิงแบบแห้งของมีเทน ได้ทำการศึกษาโดยใช้พลศาสตร์ของไหลเชิงคำนวณในขั้นแรกเรขาคณิตทรงกลมถูกพัฒนาเป็นโดเมนเพื่อจำลองรูปร่างของตัวเร่งปฏิกิริยาจริง ผลตรวจสอบความถูกต้องพบว่าการสะสมของโค้ก และการเสื่อมสภาพบนอนุภาคตัวเร่งปฏิกิริยามีผลสอดคล้องที่ดีกับผลการทดลอง ในขั้นต้น โค้กถูกสร้างขึ้นที่พื้นผิวของตัวเร่งปฏิกิริยาและค่อย ๆ ก่อตัวขึ้นที่จุดศูนย์กลาง เมื่อปฏิกิริยาดำเนินไป ความเข้มข้นของโค้กที่จุดศูนย์กลางจะสูงกว่าที่พื้นผิว ในขั้นที่สองผลกระทบของอัตราส่วนมีเทนต่อคาร์บอนไดออกไซด์ และอุณหภูมิต่อการเกิดโค้กถูกพิจารณา โปรไฟล์ความเข้มข้นที่ถูกพัฒนาขึ้นเหล่านี้สามารถนำมาใช้เพิ่มเติมความเข้าใจที่ดีขึ้นเกี่ยวกับพฤติกรรมของการก่อตัวของโค้ก ซึ่งนำไปสู่การปรับปรุงประสิทธิภาพโดยรวมสำหรับกระบวนการรีฟอร์มมิงแบบแห้งของมีเทน

สาขาวิชา วิศวกรรมเคมี
 ปีการศึกษา 2564

ลายมือชื่อนิสิต

ลายมือชื่อ อ.ที่ปรึกษาหลัก

ลายมือชื่อ อ.ที่ปรึกษาร่วม

ลายมือชื่อ อ.ที่ปรึกษาร่วม

6270052521 : MAJOR CHEMICAL ENGINEERING

KEYWORD: CFD Dry reforming of methane Coke formation

Chananun Rojanarungruengporn : PREDICTION OF COKE FORMATION OVER A CATALYST PARTICLE FOR DRY REFORMING OF METHANE. Advisor: Asst. Prof. SUPHOT PHATANASRI, Ph.D. Co-advisor: SUPAREAK PRASERTHDAM, Ph.D., PHUET PRASERTCHAROENSUK, Ph.D., KRITChart WONGWAILIKHIT, Ph.D.

Nowadays, global warming is a significant environmental problem causing various impacts across the globe. Dry reforming of methane (DRM) is one of the reactions that can utilize CO_2 effectively. However, the major problem of DRM process is the deactivation of catalysts caused by coke formation over the catalyst particle which mainly occurs from CH_4 decomposition reaction. Coke formation leads to a decrease in catalytic performance by blocking the pores and active sites. In this study, the spatial catalyst deactivation caused by coke formation over a spherical alumina-supported nickel catalyst ($\text{Ni}/\text{Al}_2\text{O}_3$) particle in dry reforming of methane (DRM) was investigated using computational fluid dynamics (CFD). Firstly, a spherical geometry was developed as the simulation domain to replicate the shape of an actual catalyst. The validation result indicated that both coke accumulation and deactivation on a catalyst particle showed a good agreement with the experimental data. The coke was initially formed at the surface of the catalyst and gradually formed at the center. As the reaction progressed, the concentration of coke at the center was higher than at the surface. Secondly, the effect of CH_4/CO_2 ratio and temperature on the coke formation was considered. These developed concentration profiles can be further used for a better understanding of coke formation behavior, leading to an improvement of the overall efficiency for the DRM process.

Field of Study: Chemical Engineering

Student's Signature

Academic Year: 2021

Advisor's Signature

Co-advisor's Signature

Co-advisor's Signature

ACKNOWLEDGEMENTS

This thesis could not be achieved without the support of several people. Firstly, the author would like to thank my advisor, Assistant Professor Suphot Phatanasri for his introducing me to this project. Furthermore, the author also would like to thank my co-advisors, Dr. Kritchart Wongwailikhit, Dr. Phuet Prasertcharoensuk, Assistant Professor Supareak Prasertthdam, Withawin Vilaivannaporn, for their helpful and valuable suggestions, supervision and encouragement throughout the course of this work. Additionally, the author is grateful to Assistant Professor Nattaporn Tonanon as the chairman of this thesis committee; Dr. Chutimon Satirpipathkul, and Associate Professor Sunun Limtrakul as the members of this thesis committee for their suggestions and valuable time devoted to review this thesis.

The author greatly thanks to the Center of Excellence on Catalysis and Catalytic Reaction Engineering, Department of Chemical Engineering, Faculty of Engineering, Chulalongkorn University, for support on this project.

Lastly, the author would like to thank my beloved parents for their endless love and support throughout my life.

TABLE OF CONTENTS

	Page
.....	iii
ABSTRACT (THAI).....	iii
.....	iv
ABSTRACT (ENGLISH).....	iv
ACKNOWLEDGEMENTS.....	v
TABLE OF CONTENTS.....	vi
LIST OF TABLES.....	x
LIST OF FIGURES.....	xi
CHAPTER I.....	1
INTRODUCTION.....	1
1.1 Motivation.....	1
1.2 Objective of Research.....	3
1.3 Scope of Research.....	3
CHAPTER II.....	5
THEORY AND LITERATURE REVIEWS.....	5
2.1 Computational fluid dynamics (CFD).....	5
2.1.1 Pre-processor.....	5
2.1.2 Solve.....	6
2.1.3 Post-processor.....	6
2.2 Governing equations.....	7
2.2.1 Conservation of mass equation.....	8

2.2.2 Conservation of momentum equation	8
2.2.3 Conservation of species transport equation.....	9
2.2.4 Conservation of energy equation.....	10
2.3 Porous media.....	11
2.3.1 Momentum equation in porous media	12
2.3.2 Darcy's law in porous media	12
2.3.3 Inertial losses in porous media.....	13
2.3.4 Relative viscosity in porous media	14
2.3.5 Species transportation equation in porous media	15
2.3.6 Energy equation in porous media.....	16
2.4 Reaction rates equations.....	17
2.5 Metal catalyst.....	19
2.6 Support	20
2.7 Literature reviews.....	21
CHAPTER III	24
EXPERIMENT	24
3.1 Grid independence test.....	25
3.2 Model validation using methane decomposition reaction	25
3.2.1 Model validation using deactivation rate	26
3.2.2 Model validation using coke formation and porosity relation.....	26
3.3 Simulation of coke formation behavior for DRM process	26
3.3.1 Mathematical model	26
3.3.1.1 Governing equations	26
3.3.1.2 Reaction kinetic model	30

3.3.2 System description and boundary condition	32
3.3.3 Assumptions	34
3.4 Study the effect of operating parameters on coke formation for the DRM reaction	34
CHAPTER IV	35
RESULTS AND DISCUSSION.....	35
4.1 Grid independence test.....	35
4.2 Model validation using methane cracking reaction.....	36
4.2.1 Model validation using deactivation rate	36
4.2.2 Model validation using coke formation and porosity relation.....	39
4.2.2.1 Model validation.....	39
4.2.2.2 Model optimization.....	46
4.3 Coke formation behavior for dry reforming of methane reaction in a catalyst particle	49
4.3.1 Concentration profile and coke formation	49
4.3.1.1 CO and H ₂ concentration.....	49
4.3.1.2 Coke accumulation	54
4.3.1.3 Porosity and effective diffusion coefficient.....	57
4.3.1.4 Temperature.....	65
4.3.2 Effect of operating parameters on coke formation and concentration profile for the DRM reaction	68
4.3.2.1 CH ₄ /CO ₂ molar ratio	68
4.3.2.2 Temperature.....	71
CHAPTER V	74
CONCLUSIONS AND RECOMMENDATIONS.....	74

5.1 Conclusions.....	74
5.2 Recommendations.....	75
REFERENCES	76
VITA.....	80



LIST OF TABLES

	Page
Table 1 Properties of nickel	19
Table 2 Properties of aluminum	20
Table 3 Kinetic parameters for the model of DRM reaction rate.....	30
Table 4 Operating conditions and physical properties used in the simulation.	33
Table 5 Grid quantity and quality for different grid size	35



LIST OF FIGURES

	Page
Figure 1 CFD processing diagram	7
Figure 2 Research methodology	24
Figure 3 A cross-section schematic of a sphere single catalyst particle geometry domain with 290265 elements	25
Figure 4 A schematic of a sphere single catalyst particle geometry domain.	33
Figure 5 Distribution of the specific coke accumulation on the catalyst particle for four sets of computational grids.	36
Figure 6 Yang et al. (points) and simulation (lines) time dependencies of specific coke accumulation on the catalyst particle.	37
Figure 7 Yang et al. (points) and simulation (lines) time dependencies of reaction rate on the catalyst particle.	37
Figure 8 Yang et al. (points) and simulation (lines) time dependencies of activity on the catalyst particle.	38
Figure 9 Yang et al. (points) and simulation (lines) time dependencies of porosity on the catalyst particle.	38
Figure 10 Zavarukhin et al. (points) and simulation (lines) time dependencies of reaction rate with different H ₂ content on the catalyst particle.	40
Figure 11 Zavarukhin et al. (points) and simulation (lines) time dependencies of reaction rate with the different temperature at 40% H ₂ content on the catalyst particle.	41
Figure 12 Time dependencies of porosity with different H ₂ content on the catalyst particle.	42
Figure 13 Time dependencies of effective diffusion coefficient with different H ₂ content on the catalyst particle.	43

Figure 14 Radius distribution of coke concentration with 20% H ₂ content on the catalyst particle at 4 sec.....	43
Figure 15 Radius distribution of coke concentration with 20% H ₂ content on the catalyst particle at 20 sec.....	44
Figure 16 Radius distribution of coke concentration with 20% H ₂ content on the catalyst particle at 2000 sec.	44
Figure 17 The instantaneous contour of coke accumulation with 20% H ₂ content on the catalyst particle at (a) 4 sec (b) 20 sec (c) 2000 sec.....	45
Figure 18 Zavarukhin et al. (points) and simulation (lines) time dependencies of reaction rate with different coke density at 20% H ₂ content and pore size of 15 nm on the catalyst particle.....	47
Figure 19 Zavarukhin et al. (points) and simulation (lines) time dependencies of reaction rate with different catalyst pore size at 20% H ₂ content and coke density of 2.36 kg/m ³ on the catalyst particle.....	47
Figure 20 Time dependencies of CO concentration on the catalyst particle for DRM.	49
Figure 21 Time dependencies of H ₂ concentration on the catalyst particle for DRM.	50
Figure 22 The instantaneous contour of CO concentration inside the particle at (a) 20 sec (b) 200 sec (c) 2000 sec (d) 10000 sec.....	52
Figure 23 The instantaneous contour of H ₂ concentration inside the particle at (a) 20 sec (b) 200 sec (c) 2000 sec (d) 10000 sec.....	53
Figure 24 Time dependencies of coke accumulation on the catalyst particle for DRM.	54
Figure 25 The instantaneous contour of coke accumulation inside the particle at (a) 20 sec (b) 2000 sec (c) 10000 sec (d) 50000 sec.....	55
Figure 26 Radius distribution of coke concentration on the catalyst particle for DRM at 20 sec.....	56

Figure 27 Radius distribution of coke concentration on the catalyst particle for DRM at 2000 sec.....	56
Figure 28 Radius distribution of coke concentration on the catalyst particle for DRM at 10000 sec	57
Figure 29 Time dependencies of porosity on the catalyst particle for DRM.	57
Figure 30 Time dependencies of effective diffusion coefficient on the catalyst particle for DRM.	58
Figure 31 The instantaneous contour of porosity inside the particle at (a) 20 sec (b) 2000 sec (c) 10000 sec (d) 50000 sec.....	60
Figure 32 The instantaneous contour of effective diffusion coefficient inside the particle at (a) 20 sec (b) 2000 sec (c) 10000 sec (d) 50000 sec.	61
Figure 33 Radius distribution of porosity on the catalyst particle for DRM at 20 sec..	62
Figure 34 Radius distribution of porosity on the catalyst particle for DRM at 2000 sec.	62
Figure 35 Radius distribution of porosity on the catalyst particle for DRM at 10000 sec	63
Figure 36 Radius distribution of effective diffusion coefficient on the catalyst particle for DRM at 20 sec.	63
Figure 37 Radius distribution of effective diffusion coefficient on the catalyst particle for DRM at 2000 sec.....	64
Figure 38 Radius distribution of effective diffusion coefficient on the catalyst particle for DRM at 10000 sec.....	64
Figure 39 The instantaneous contour of temperature inside the particle at (a) 20 sec (b) 2000 sec (c) 10000 sec (d) 50000 sec.	66
Figure 40 Radius distribution of temperature on the catalyst particle for DRM at 20 sec.....	67

Figure 41 Radius distribution of temperature on the catalyst particle for DRM at 2000 sec.....	67
Figure 42 Radius distribution of temperature on the catalyst particle for DRM.....	68
Figure 43 Time dependencies of coke accumulation on the catalyst particle for DRM with different CH_4/CO_2 molar ratios.....	69
Figure 44 Time dependencies of H_2 concentration on the catalyst particle for DRM with different CH_4/CO_2 molar ratios.....	69
Figure 45 Time dependencies of CO concentration on the catalyst particle for DRM with different CH_4/CO_2 molar ratios.....	70
Figure 46 Time dependencies of coke accumulation on the catalyst particle for DRM with different temperatures.....	71
Figure 47 Time dependencies of H_2 concentration on the catalyst particle for DRM with different temperatures.....	72
Figure 48 Time dependencies of CO concentration on the catalyst particle for DRM with different temperatures.....	72

CHAPTER I

INTRODUCTION

1.1 Motivation

Nowadays, global warming is a serious environmental problem caused by the emission of greenhouse gases into the atmosphere, and the impacts of its have an effect across the globe[1]. The main components of greenhouse gases are carbon dioxide (CO₂) and methane (CH₄) which are mainly produced by human activities, cutting down forests and burning fossil fuels such as oil, coal, and gas in industries.



Catalytic reforming technology has been widely used in industries since the 1960s. Dry reforming of methane (DRM) (Eq. 1) is one of the methods that can be converted the two main greenhouse gases into synthetic gas (known as syngas) [2]. DRM solid-catalyzed gas-phase reaction is carried out in a packed bed reactor. The theoretical H₂/CO molar ratio produced by the DRM process is close to 1, which can be converted further into synthetic liquid fuels (diesel fuel and gasoline) and valuable chemicals (i.e. methanol, ethanol, and alcohol) via Fischer-Tropsch processes [3]. DRM reaction (Eq. 1) is a highly endothermic reaction; therefore, it requires a high temperature at 500-1000 °C and a high energy supply. However, the major problem of the DRM process is the deactivation of the catalyst caused by coke formation and crystallite agglomeration during the DRM process. Although noble

metals catalysts such as platinum (Pt), ruthenium (Ru), and rhodium (Rh) have high activity and good stability for reforming reaction, they are not suitable for industrial due to low availability and high cost. Nickel (Ni) catalyst, especially nickel supported on alumina ($\text{Ni}/\text{Al}_2\text{O}_3$), is the most useful in the DRM process because of its low cost and suitable activity. However, Nickel catalysts are easier to coke formation compare to noble metals catalysts. Coke formation mainly occurs from the CH_4 decomposition reaction (Eq. 2) leads to a decrease in catalytic performance by blocking the pores and active sites [4, 5]. Furthermore, these side reactions also alter the ratio of H_2/CO in the reactor from its optimal condition [6].

Common particle shapes that are used in packed bed reactors are sphere and cylinder, and other shapes with either internal or external voids are also used due to their high surface-area-to-volume ratio. Particle shape is a crucial parameter that could affect the fluid flow around a particle which affects the heat transfer, mass transfer, and chemical reactions [7]. Thus, it is necessary to study the coke formation behavior, to better understand the catalyst deactivation of heterogeneous type catalyst particles in the DRM process.

Computational fluid dynamics (CFD) is considered an efficient design tool to simulate and investigate the fluid flow pattern, chemical reaction, heat transfer, and related transport phenomena to optimize operating conditions of DRM reaction or design and optimize a new catalyst bed reactor. It can be used to predict scale-up behavior, therefore, reduce engineering cost and process development time from laboratory to pilot/industrial scales. Several studies on simulation of DRM have been carried out in literature [8-10]. However, there are only a few workers have been focusing on the coke formation behaviors on a catalyst particle in the DRM process.

The objectives of this study are to investigate the carbon formation behavior over a sphere alumina-supported nickel catalyst ($\text{Ni}/\text{Al}_2\text{O}_3$) particle for DRM process and to study the effect of operating parameters on coke formation. The three-dimensional (3D) CFD simulation with the chemical reactions is provided by

commercial software FLUENT. The simulation results were compared with the experimental data to validate the CFD mathematical model. The detailed CFD presented here can contribute to a better understanding of carbon formation behavior, which might lead to the improvement of the overall efficiency of the DRM process.

1.2 Objective of Research

To develop the mathematical model for coke formation over a catalyst particle for dry reforming of methane.

1.3 Scope of Research

The scope of research is as follows:

- 1.3.1 This work predicts atomic coke formation over a sphere alumina-supported nickel catalyst ($\text{Ni}/\text{Al}_2\text{O}_3$) particle for dry reforming of methane (DRM)
- 1.3.2 A sphere single catalyst particle model was used with a particle diameter of 2 mm, particle pore diameter of 15 nm, initial pellet porosity of 0.45.
- 1.3.3 The coke formation over a sphere $\text{Ni}/\text{Al}_2\text{O}_3$ catalyst particle for DRM process, including model validation using experimental and available literature data.
- 1.3.4 The operating conditions for the DRM process simulation were set reaction temperature of 500 °C, pressure inlet of 0.1 MPa, $\text{CH}_4/\text{CO}_2/\text{He}$ molar ratio of 0.15/0.15/0.7.

- 1.3.5 The CH_4/CO_2 molar ratio was varied with the feed composition of 0.15/0.15, 0.15/0.075, and 0.075/0.15 to study the effect of operating parameters on coke formation in the DRM process.
- 1.3.6 The reaction temperature of 500, 550, and 600 was varied to study the effect of operating parameters on coke formation in the DRM process.



CHAPTER II

THEORY AND LITERATURE REVIEWS

2.1 Computational fluid dynamics (CFD)

Computational fluid dynamics or CFD is one of the techniques that used the numerical solution methods applied to analyze and solve fluid flow, heat transfer, chemical reaction, and related phenomena problems. FLUENT software is one of the most popular CFD solvers that can analyze a range of problems related to laminar and turbulent flows, incompressible and compressible fluids and multiphase flows, etc. CFD is an important engineering tool, which can provide clear insight into many fluid flow phenomena with inexpensive operating costs, to help researchers to get a better understanding of the flow phenomena. CFD simulation involves the use of the conservation law including mass, momentum, and energy equations. The additional equation can also be added into the calculation model to better representation of the problems. CFD can be applied to a wide range of industrial and non-industrial applications.

CFD analysis consists of three main processes, including pre-processor, solver, and post-processor as shown in Fig. 1.

2.1.1 Pre-processor

Pre-processing is the first step in CFD simulation. It consists of (a) creating the geometry of interest domain either 2D or 3D model for CFD simulation, and (b) creating small cells in the domain (known as meshing). In this step, physical and chemical properties of operating parameters, material property, initial and boundary conditions, and other related variables are defined.

2.1.2 Solve

Solving step is to numerically solve the fluid flow equations in the computational domain using the CFD solver. There are three distinct streams of numerical solution techniques: (a) finite difference, (b) finite element, and (C) finite volume methods. This study mainly focused on fluid dynamics analysis. Therefore, the finite volume method was chosen for this study. The concept of the finite volume method is as follows:

- Integration of the governing equations over all the control volume of the domain
- Transform the PDEs into algebraic equations. This step is called discretization.
- Applying an iterative method to solve the algebraic equations.

2.1.3 Post-processor

After the solving step is completed, the simulation results are visualized and analyzed in the post-processing step using reports, vector plots, line and shaded contour plots and animations, etc.

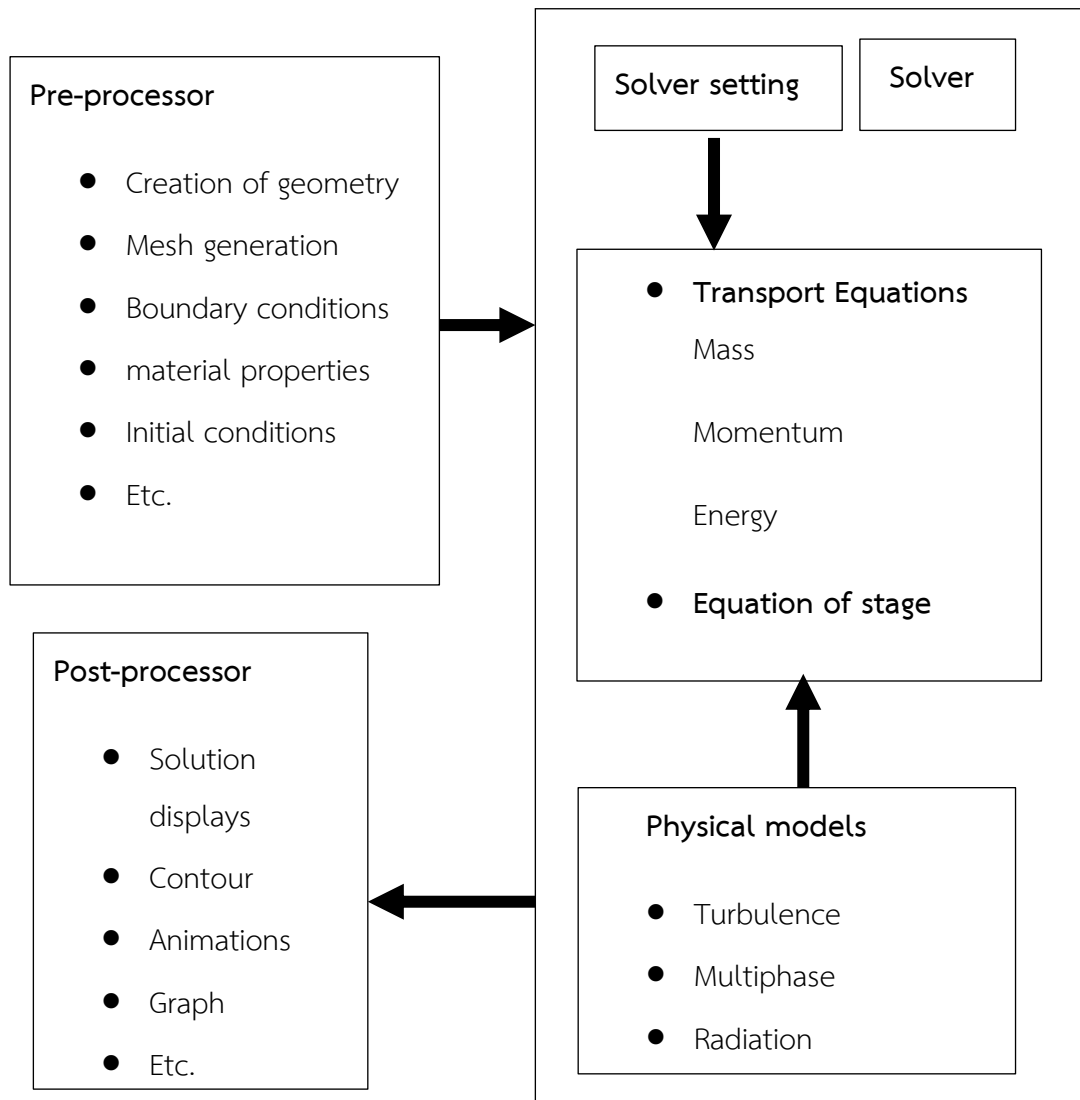


Figure 1 CFD processing diagram

2.2 Governing equations

CFD is fundamentally based on the governing equations of fluid dynamics, including conservation of mass, momentum, and energy.

2.2.1 Conservation of mass equation

The conservation of mass or continuity equation is given by:

$$\frac{\partial \rho}{\partial t} + (\nabla \cdot \rho \mathbf{v}) = 0 \quad (\text{Eq. 3})$$

where ρ is the density, \mathbf{v} is the velocity, and ∇ is the gradient operator.

or

$$\frac{\partial \rho}{\partial t} + \frac{\partial}{\partial x}(\rho v_x) + \frac{\partial}{\partial y}(\rho v_y) + \frac{\partial}{\partial z}(\rho v_z) = 0 \quad (\text{Eq. 4})$$

where v_x , v_y and v_z are the velocity along the x, y, and z-axis, respectively.

If the density is constant, the continuity equation reduces to:

$$\frac{\partial}{\partial x}(v_x) + \frac{\partial}{\partial y}(v_y) + \frac{\partial}{\partial z}(v_z) = 0 \quad (\text{Eq. 5})$$

2.2.2 Conservation of momentum equation

Conservation of momentum equation or Newton's second law which can be referred to as the Navier-Stokes Equation is given by:

$$\frac{\rho D\mathbf{v}}{Dt} = -\nabla P - [\nabla \cdot \boldsymbol{\tau}] + \rho \mathbf{g} \quad (\text{Eq. 6})$$

where P is static pressure, $\boldsymbol{\tau}$ is viscous stress tensor and $\rho \mathbf{g}$ is the gravitational force per unit volume. The x, y, and z components of the momentum equations are shown in Eq.7, 8, and 9, respectively.

x-component:

$$\begin{aligned} & \rho \left(\frac{\partial v_x}{\partial t} + v_x \frac{\partial v_x}{\partial x} + v_y \frac{\partial v_x}{\partial y} + v_z \frac{\partial v_x}{\partial z} \right) \\ &= -\frac{\partial P}{\partial x} - \left[\frac{\partial}{\partial x} \tau_{xx} + \frac{\partial}{\partial y} \tau_{yx} + \frac{\partial}{\partial z} \tau_{zx} \right] + \rho g_x \quad (\text{Eq. 7}) \end{aligned}$$

y-component:

$$\begin{aligned} & \rho \left(\frac{\partial v_y}{\partial t} + v_x \frac{\partial v_y}{\partial x} + v_y \frac{\partial v_y}{\partial y} + v_z \frac{\partial v_y}{\partial z} \right) \\ &= -\frac{\partial P}{\partial y} - \left[\frac{\partial}{\partial x} \tau_{xy} + \frac{\partial}{\partial y} \tau_{yy} + \frac{\partial}{\partial z} \tau_{zy} \right] + \rho g_y \quad (\text{Eq. 8}) \end{aligned}$$

z-component:

$$\begin{aligned} & \rho \left(\frac{\partial v_z}{\partial t} + v_x \frac{\partial v_z}{\partial x} + v_y \frac{\partial v_z}{\partial y} + v_z \frac{\partial v_z}{\partial z} \right) \\ &= -\frac{\partial P}{\partial z} - \left[\frac{\partial}{\partial x} \tau_{xz} + \frac{\partial}{\partial y} \tau_{yz} + \frac{\partial}{\partial z} \tau_{zz} \right] + \rho g_z \quad (\text{Eq. 9}) \end{aligned}$$

2.2.3 Conservation of species transport equation

The conservation equation for the chemical species is given by:

$$\frac{\partial(\rho Y_i)}{\partial t} + \nabla \cdot (\rho \vec{v} Y_i) = -\nabla \cdot \vec{J}_i + R_i \quad (\text{Eq. 10})$$

where Y_i is the local mass fraction of each species, J_i is the diffusion flux of species i , and R_i is the net rate of production of species i by chemical reaction. The diffusion flux of species i can be determined from Eq. 11 or Eq. 12.

Mass diffusion in laminar flows:

$$\vec{J}_i = -\rho D_{i,m} \nabla Y_i - D_{T,i} \frac{\nabla T}{T} \quad (\text{Eq. 11})$$

Mass diffusion in turbulent flows:

$$\vec{J}_i = -\left(\rho D_{i,m} + \frac{\mu_t}{Sc_t}\right) \nabla Y_i - D_{T,i} \frac{\nabla T}{T} \quad (\text{Eq. 12})$$

where $D_{i,m}$ is the mass diffusion coefficient for species i in the mixture, $D_{T,i}$ is the thermal diffusion coefficient, Sc_t is the turbulent Schmidt number, and μ_t is the turbulent viscosity.

2.2.4 Conservation of energy equation

Conservation of energy is the first law of thermodynamics which states that the sum of the work and heat added to the system.

$$dE = dQ + dW \quad (\text{Eq. 13})$$

where dQ is the heat added to the system, dW is the work done on the system and dE is the increment in the total energy of the system. Energy equations can be written in many different ways. One of the common types of an energy equation is:

$$\rho \left[\frac{\partial h}{\partial t} + \nabla \cdot (h\nu) \right] = -\frac{DP}{Dt} + \nabla \cdot (k\nabla T) + \phi \quad (\text{Eq. 14})$$

where h is the specific enthalpy that is related to specific internal energy. ∇T is the absolute temperature and ϕ is the dissipation function representing the work done against viscous forces, which is irreversibly converted into internal energy.

2.3 Porous media

A porous media model incorporates an empirically determined flow resistance in a region of the model defined as porous. The porous media model is an additional term of momentum sink in the governing momentum equations. A porous media consists of a network of pores contained in material or some control volume. The volume fraction between the void and the solid in a material is more significant than the mass fraction of the material for calculation. The volume fraction presented in a material or a control volume is referred to as the porosity which is a dimensionless variable with values that range from 0 to 1. Porosity can be calculated as:

$$\varepsilon = \frac{V_{pore}}{V_{CV}} \quad (\text{Eq. 15})$$

where ε is the porosity, V_{pore} is the volume of the pores existing in a material, and V_{CV} is the volume of the control volume.

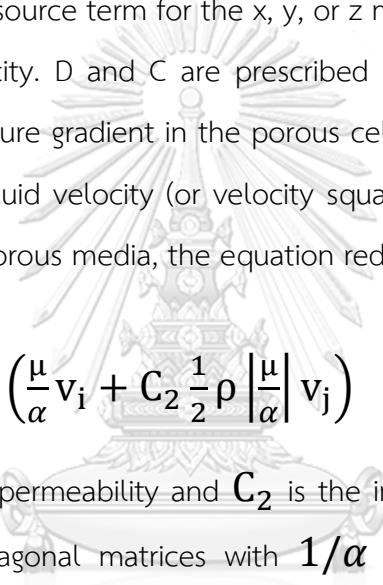
2.3.1 Momentum equation in porous media

Porous media are modeled by the addition of a momentum source term to the standard fluid flow equations. The source term is composed of two parts which are a viscous loss term and an internal loss term shown in Eq.16.

$$S_i = - \left(\sum_{j=1}^3 D_{ij} \mu v_j + \sum_{j=1}^3 C_{ij} \frac{1}{2} \rho |v| v_j \right) \quad (\text{Eq. 16})$$

where S_i is the source term for the x, y, or z momentum equation, $|v|$ is the magnitude of the velocity. D and C are prescribed matrices. This momentum sink contributes to the pressure gradient in the porous cell, creating a pressure drop that is proportional to the fluid velocity (or velocity squared) in the cell. In the case of simple homogeneous porous media, the equation reduces to:

$$S_i = - \left(\frac{\mu}{\alpha} v_i + C_2 \frac{1}{2} \rho \left| \frac{\mu}{\alpha} v_j \right| v_j \right) \quad (\text{Eq. 17})$$

where α is the permeability and C_2 is the inertial resistance factor, Simple specify D and C as diagonal matrices with $1/\alpha$ and C_2 , respectively, on the diagonals (and zero for the other elements) 

2.3.2 Darcy's law in porous media

In laminar flows through porous media, the pressure drop is typically proportional to velocity and the constant C_2 can be considered to be zero. Ignoring convection acceleration and diffusion, the porous media model then reduced to Darcy's law:

$$\nabla p = - \frac{\mu}{\alpha} \vec{v} \quad (\text{Eq. 18})$$

The pressure drop in each of the x, y, z directions within the porous region is:

x-component:

$$\Delta p_x = \sum_{j=1}^3 \frac{\mu}{\alpha_{xj}} v_j \Delta n_x \quad (\text{Eq. 19})$$

y-component:

$$\Delta p_y = \sum_{j=1}^3 \frac{\mu}{\alpha_{yj}} v_j \Delta n_y \quad (\text{Eq. 20})$$

z-component:

$$\Delta p_z = \sum_{j=1}^3 \frac{\mu}{\alpha_{zj}} v_j \Delta n_z \quad (\text{Eq. 21})$$

Where $1/\alpha_{ij}$ are the entries in the matrix D, \mathbf{v}_j are the velocity components in the x, y, and z directions, and Δn_x , Δn_y , Δn_z are the thickness of the medium in the x, y, and z directions.

2.3.3 Inertial losses in porous media

At high flow velocity, the constant C_2 in the equation provides a correction for inertial losses in the porous medium. This constant can be viewed as a loss coefficient per unit length along the flow direction, thereby allowing the pressure drop to be specified as a function of the dynamic head. For a perforable plated or tube bank, the permeability term can be eliminated and the inertial term can be used alone, yielding the following simplified form of the porous media equation:

$$\nabla p = - \sum_{j=1}^3 C_{2ij} \left(\frac{1}{2} \rho v_j |v| \right) \quad (\text{Eq. 22})$$

or when written in terms of the pressure drop in the x, y, z directions:

x-component:

$$\Delta p_x \approx \sum_{j=1}^3 C_{2_{xj}} \Delta n_x \frac{1}{2} \rho v_j |v| \quad (\text{Eq. 23})$$

y-component:

$$\Delta p_y \approx \sum_{j=1}^3 C_{2_{yj}} \Delta n_y \frac{1}{2} \rho v_j |v| \quad (\text{Eq. 24})$$

z-component:

$$\Delta p_z \approx \sum_{j=1}^3 C_{2_{zj}} \Delta n_z \frac{1}{2} \rho v_j |v| \quad (\text{Eq. 25})$$

2.3.4 Relative viscosity in porous media

For viscous flows, an effective viscosity, μ_e , is introduced to account for the effect of the porous medium on the diffusion term in the momentum equation:

$$\mu_e = \mu_r \mu \quad (\text{Eq. 26})$$

where μ is the fluid viscosity and μ_r is the relative viscosity.

Brinkman correction

$$\mu_r = (1 - \gamma)^{-2.5} \quad (\text{Eq. 27})$$

Einstein formula

$$\mu_r = 1 + 2.5(1 - \gamma) \quad (\text{Eq. 28})$$

Breugem correction

$$\mu_r = \begin{cases} \frac{1}{2} \left(\gamma - \frac{3}{7} \right) & \gamma \geq \frac{3}{7} \\ 0 & \gamma < \frac{3}{7} \end{cases} \quad (\text{Eq. 29})$$

2.3.5 Species transportation equation in porous media

The conservation equation for the chemical species inside the porous media is given by:

$$\varepsilon \rho \frac{\partial \omega_i}{\partial t} - \nabla \cdot \left(\rho D_i^{eff} \nabla \omega_i + \rho D_i^{eff} \frac{\nabla M_n}{M_n} - \rho \omega_i \sum_k \frac{M_i}{M_n} D_k^{eff} \nabla x_k \right) = R_i \quad (\text{Eq. 30})$$

where M_n is the average molar weight, R_i is the reaction source, and D_i^{eff} is the effective diffusion coefficient. The effective diffusion coefficient which depends on the porosity ε and tortuosity τ can be calculated by the Knudsen diffusion ($D_{i,k}$) and molecular diffusion ($D_{i,j}$):

$$D_i^{eff} = \varepsilon^2 \frac{D_{i,j} \cdot D_{i,k}}{D_{i,j} + D_{i,k}} \quad (\text{Eq. 31})$$

The Knudsen diffusion is shown in Eq. 32, where \bar{r}_p is the averaged pore diameter.

$$D_{i,k} = 97\bar{r}_p \left(\frac{T}{M_i}\right)^{\frac{1}{2}} \quad (\text{Eq. 32})$$

The molecular diffusion, which is shown in Eq. 33, is calculated by the Fuller equation.

$$D_{i,j} = \frac{1 \times 10^{-7} T^{1.75} \left(\frac{1}{M_i} + \frac{1}{M_j}\right)^{\frac{1}{2}}}{P(v_i^{1/3} + v_j^{1/3})^{\frac{1}{2}}} \quad (\text{Eq. 33})$$

The change of porosity ε is associated with the coke deposition rate, which can be described as below [11]:

$$\varepsilon = \varepsilon_0 - \frac{r_c M_c}{\rho_c} \Delta t \quad (\text{Eq. 34})$$

Where ε_0 is the initial porosity, ρ_c is the and M_c is the molar weight of coke.

2.3.6 Energy equation in porous media

The standard energy equation in porous media, which is shown in Eq. 35, is modified to include the conduction flux and the transient term. Effective conductivity is used for the conduction flux, and in the transient term, the thermal inertia of the solid phase is also considered.

$$\begin{aligned} & \frac{\partial}{\partial t} (\varepsilon \rho_f E_f + (1 - \varepsilon) \rho_s E_s) + \nabla \cdot (\vec{v} (\rho_f E_f + P)) \\ & = \nabla \cdot [k_{eff} \nabla T - (\sum_i h_i \vec{j}_i)] + S_f^h \end{aligned} \quad (\text{Eq. 35})$$

Where E_f is the total fluid energy, E_s is the total solid medium energy, S_f^h is the fluid enthalpy source term, h_i is the enthalpy of the species, and k_{eff} is the effective thermal conductivity. In addition, the effective thermal conductivity in porous media is defined as:

$$k_{eff} = \varepsilon k_f + (1 - \varepsilon)k_s \quad (\text{Eq. 36})$$

2.4 Reaction rates equations

The DRM and CH_4 decomposition reactions are shown in Eq. 37 and Eq. 38, respectively.



the rate expression in a Langmuir-Hinshelwood mechanism developed by Wang et al. (1999) [12] can be used to describe the DRM reaction as below:

$$r = \frac{k_1 P_{\text{CH}_4} P_{\text{CO}_2}}{(1 + K_1 P_{\text{CH}_4})(1 + K_2 P_{\text{CO}_2})} \quad (\text{Eq. 39})$$

The corresponding reaction rate with the catalyst deactivation of CH₄ decomposition reaction developed by and Zavarukhin et al. (2004) [13], which is adopted to realize the coke deposition process in DRM is described as follows:

$$r = a \cdot r_c \max \quad (\text{Eq. 40})$$

$$r_c \max = k \frac{p_{CH_4} - p_{H_2}/K_p}{(1 + k_H \sqrt{p_{H_2}})^2} \quad (\text{Eq. 41})$$

$$k = \exp \left(20.492 - \frac{104200}{RT} \right) \quad (\text{Eq. 42})$$

$$K_p = 5.088 \times 10^5 \exp \left(-\frac{91200}{RT} \right) \quad (\text{Eq. 43})$$

$$k_H = \exp \left(\frac{163200}{RT} - 22.426 \right) \quad (\text{Eq. 44})$$

$$k_a = \exp \left(\frac{135600}{RT} - 32.077 \right) \quad (\text{Eq. 45})$$

Where r_c is the rate of coke production. c is specific coke content on the catalyst, depending on time, temperature, partial pressures of methane, p_{CH_4} , and hydrogen, p_{H_2} , and the type of catalyst. a is relative catalyst activity. k_H and K_p are the equilibrium constants. k and k_a are specific rate constant and deactivation rate constant, respectively.

2.5 Metal catalyst

2.5.1 Nickel (Ni)

Nickel a silvery-white metal is commonly used for utilizing as a catalyst in various industries. Nickel is a fairly good conductor of heat and highly resistant to rusting and corrosion. Nickel is a member of group 8B in the Periodic Table. In nature, many oxidation numbers are found: 0, +1, +2, +3, and +4, but generally, they are most stable in the form of a +2 charge.

Table 1 Properties of nickel

Properties	
Name	Nickel
Atomic Symbol	Ni
Atomic Number	28
Atomic weight	58.6934 g/mol
Element Category	Transition metal
Oxidation States	0, +1, +2, +3
Density	8.908 g/cm ³
Melting Point	1,455 °C
Boiling Point	2,913 °C

2.6 Support

2.6.1 Aluminum (Al)

Alumina or aluminium oxide is a chemical compound of aluminum and oxygen with the chemical formula Al_2O_3 . It has several names such as aloxide, alundum, or aloxite depending on applications, and several occurring forms of aluminium oxide, which aluminium(III) oxide is the most common form. There are many different types of crystal structure, such as α , γ , χ , κ , δ , θ , ρ , and η -alumina. γ -alumina is widely used as commercial support and catalyst for industry and laboratory because of its moderately high surface area and stable phase in a wide range of reaction temperatures.

Table 2 Properties of aluminum

Properties	
Name	Nickel
Atomic Symbol	Ni
Atomic Number	28
Atomic weight	58.6934 g/mol
Element Category	Transition metal
Oxidation States	0, +1, +2, +3
Density	8.908 g/cm ³
Melting Point	1,455 °C
Boiling Point	2,913 °C

2.7 Literature reviews

Yang, Wang et al. (2021) [14] studied coke deposition processes inside a single catalyst particle in a fixed bed reactor. The simulation is investigated by means of a particle-resolved CFD model focusing on the change of catalyst tortuosity and physical property including initial porosity and particle diameter on coke deposition rate, porosity, and catalyst activity. The results show that the degree of reaction rate from the core to the shell will shift during the catalyst deactivation process. At the start stage, the reaction rate in the shell zone is greater. Once the carbon is accumulated, the reaction rate in the core zone is dominant. According to gas diffusion inside the catalyst, the diffusion effect is more significant at the start stage. With the decreasing catalyst activity, the diffusion effect is weakened. A larger initial particle porosity and a smaller particle diameter are easily deactivated. In addition, the wall effect on coke accumulation in a fixed bed is revealed. Moreover, more coke is formed near the wall with lower catalyst activity.

Snoeck, Froment et al. (1997) [15] derived a rigorous kinetic model for the formation of filamentous carbon on a nickel catalyst by methane cracking. The derivation of the kinetic models, based on a detailed description of the mechanism of carbon filament formation. The experimental study was performed in an electron balance unit at the temperature range of 773-823 K and the partial pressure of methane in the range of 1.5 -10 bar. The results show a very good agreement between the experimental and modeling data. The rate-determining step is the abstraction of the first hydrogen atom from molecularly adsorbed methane with the formation of an adsorbed methyl group. The rigorous kinetic modeling with the incorporation of the diffusion step allows explaining the deactivation of carbon filament growth and the influence of the affinity for carbon formation on the nucleation of filamentous carbon.

Wehinger, Eppinger, et al. (2015) [16] simulated the dry reforming of methane in spatially resolved in a fixed-bed reactor containing spheres, cylinders, and one-hole cylinders with dimensions typical for industrial applications. A better understanding of catalytic reactors is presented, which might lead to a better reactor design. The detailed fluid dynamics are coupled with detailed kinetics involving adsorption and desorption steps and reactions on the surface. The results show that the fixed bed consisting of cylindrical particles shows the highest conversions and yields. Furthermore, it shows the lowest fractions of surface adsorbed carbon which is an indicator for catalyst deactivation. On the one hand, the one-hole cylinder packing exhibits a low performance. With the modeling results, the effect of different particle shapes on transport phenomena can be quantified.

Froment and Bischoff et al. (1990) [17] discussed the problems using models that treat catalyst deactivation caused by the coke formation as a simple function of time. The results show that different reaction conditions would result in different values of the constant activity and that the constant is the function of reaction conditions. Furthermore, they argued that expressions showing the activity as a function of the coke content are more useful than the function of time.

Snoeck et al. (2003) [18] presented a linear work on the simulation of carbon formation based on their kinetic models from Snoeck et al. [11, 12] They studied the risk of carbon formation, thermodynamic and criteria comparison for different catalysts in methane steam reforming reaction. The simulation results show an accurate determination of the minimum amount of steam or the maximum amount of CO₂ that can be related to the feed. Moreover, the results showed that due to consumption of the hydrogen by reverse water gas shift reaction, the addition of CO₂ causes of higher risk for carbon formation, and a low catalyst activity leads to a higher risk of carbon formation by methane cracking, significantly at the surface of the catalysts.

Karthik and Buwa et al. (2020) [7] investigated the effect of particle shape using internally and externally- shaped particles for solid-catalyzed gas-phase reactions, i.e. methane steam reforming (MSR), water–gas shift (WGS), and methanol (MeOH), and dimethyl ether (DME) synthesis in a fixed-bed reactor. For all the reactions, the pressure drop values were found to increase with the particle surface area as it created more tortuous paths for the flow, while the temperature and species (reactants and products) concentration gradients were found to decrease with an increase in the particle surface area due to the shorter diffusion length. Therefore, the increase in the particle surface area decreased the diffusion limitation. In summary, the particle shape was found to have a considerable influence on the reaction performance and the optimal particle shape for the overall efficiency of the process depends on the extent of mass transfer limitation and reaction equilibrium for a particular reaction. The shape for the MSR and DME and the daisy shape for the WGS and MeOH were optimal for the overall reactor efficiency.

CHAPTER III

EXPERIMENT

This chapter describes the details of the experiment. Research Methodology shows in Fig. 2.

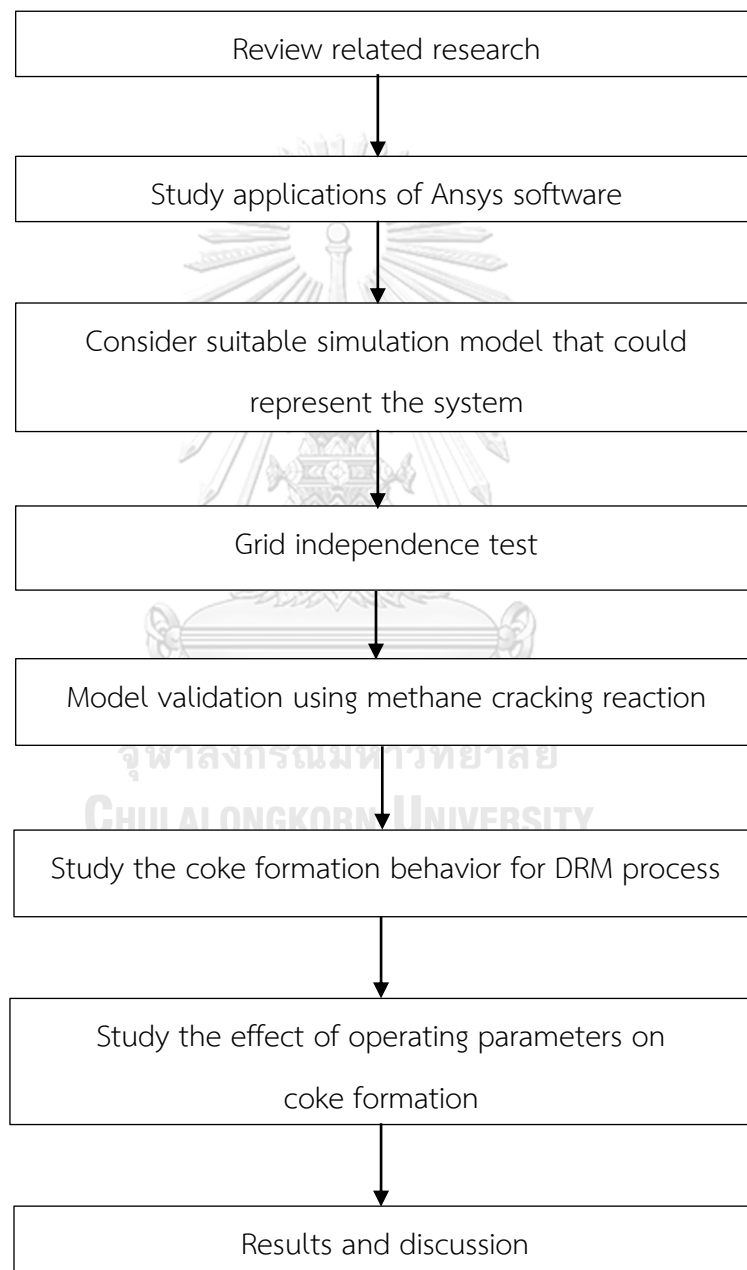


Figure 2 Research methodology

The procedures of CFD simulation consists of four sections which are: (i) Grid independence test (ii) Validation of the model (ii) Simulation of coke formation behavior for DRM process and (iv) Study the effect of operating parameters on coke formation

3.1 Grid independence test

A grid independence test was performed in order to find out the optimum grid size for the study. The cross-section schematic of a sphere single catalyst particle geometry domain is shown in Fig.3 A grid independence study was carried out at various grid numbers of 290,265, 222,953, 176,475, 114,488 elements to compare the results of specific coke accumulation distribution on the catalyst particle.

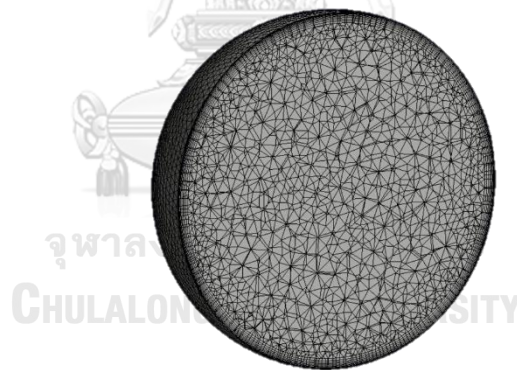


Figure 3 A cross-section schematic of a sphere single catalyst particle geometry domain with 290265 elements

3.2 Model validation using methane decomposition reaction

The model validation consists of two sections. First, the prototype model is validated using the deactivation rate to ensure that the model prediction is accurate. After that, instead of using the deactivation rate, the relationship

between porosity change and coke formation on a catalyst particle was used to develop a model that could predict coke formation in other reactions without relying on the deactivation rate.

3.2.1 Model validation using deactivation rate

The objective of validation is to ensure that the model prediction is precise. The validated model can be used as a prototype for system design and modification. The common method for validation is comparing experimental and simulated results. In the first section, to validate the CFD model the experimental results obtained from Yang et al. (2021) [14] are applied.

3.2.2 Model validation using coke formation and porosity relation

In the second section, the model was assumed that the deactivation of catalyst is only caused by coke formation which blocks porosity on a catalyst particle. To develop the model to predict coke formation in the DRM process, the relationship between porosity change and coke formation on a catalyst particle was used instead of the deactivation equation. The suggested model was checked using experimental data reported by Zavarukhin et al. (2004) [13].

3.3 Simulation of coke formation behavior for DRM process

3.3.1 Mathematical model

3.3.1.1 Governing equations

The 3D computational model is adopted to simulate coke formation behaviors from the DRM process over the Ni/Al₂O₃ catalyst. The governing equations are expressed by the following equations:

Continuity equation:

$$\frac{\partial \varepsilon \rho}{\partial t} + (\nabla \cdot \varepsilon \rho \vec{v}) = 0 \quad (\text{Eq. 46})$$

Where \vec{v} is the velocity and ε is the porosity of the medium defined as the ratio of volume fraction between the void and the total volume.

Momentum conservation equation:

$$\frac{\partial}{\partial t} (\varepsilon \rho \vec{v}) + \nabla \cdot (\varepsilon \rho \vec{v} \vec{v}) = -\varepsilon \nabla p + \nabla \cdot (\varepsilon \bar{\tau}) + \varepsilon \vec{B}_f - \left(\frac{\varepsilon^2 \mu}{K} \vec{v} + C_2 \frac{\varepsilon^3}{2} \rho |\vec{v}| \vec{v} \right) \quad (\text{Eq. 47})$$

Where p is the static pressure, $\bar{\tau}$ is the stress tensor, α is the permeability and C_2 is the inertial resistance factor. In laminar flows through porous media, the pressure drop is typically proportional to velocity and the constant C_2 can be considered to be zero. In the porous media, diffusion of gas species takes place as a result of a concentration gradient that drove the diffusive movement. Therefore, the diffusion term is significant in porous media while the convection term, which is the second term on the momentum equation, is negligible. The stress tensor is given by:

$$\bar{\tau} = \mu [(\nabla \vec{v} + \nabla \vec{v}^T) - \frac{2}{3} \nabla \cdot \vec{v} \mathbf{I}] \quad (\text{Eq. 48})$$

Where μ is the molecular viscosity, \mathbf{I} is the unit tensor, and the second term on the right-hand side is the effect of volume dilation.

Energy conservation equation:

$$\frac{\partial}{\partial t} (\varepsilon \rho_f E_f + (1 - \varepsilon) \rho_s E_s) + \nabla \cdot (\vec{v} (\rho_f E_f + p)) = S_f^h + \nabla \cdot [k_{eff} \nabla T - (\sum_j h_j J_j) + (\bar{v}_{eff} \cdot \vec{v})] \quad (\text{Eq. 49})$$

Where E_f is the total fluid energy, E_s is the total solid medium energy, ρ_f is the fluid density, ρ_s is the solid medium density and S_f^h is the fluid enthalpy source term which can be calculated by using enthalpy of the reaction shown in Eq. 57 and Eq. 58. Energy transport has been conventionally considered as combined heat flows. The significant heat transfer terms in porous media thermal conduction term, the heat of reaction term, and fluid enthalpy source term. The effective thermal conductivity in the porous medium, k_{eff} , is computed by the volume average of the fluid conductivity and the solid conductivity:

$$k_{eff} = \varepsilon k_f + (1 - \varepsilon) k_s \quad (\text{Eq. 50})$$

Where k_f is the fluid phase thermal conductivity and k_s is the solid medium thermal conductivity.

Species transportation equation:

$$\varepsilon \rho \frac{\partial \omega_i}{\partial t} - \nabla \cdot \left(\rho D_i^{eff} \nabla \omega_i + \rho D_i^{eff} \frac{\nabla M_n}{M_n} - \rho \omega_i \sum_k \frac{M_i}{M_n} D_k^{eff} \nabla x_k \right) = R_i \quad (\text{Eq. 51})$$

Where M_n is the average molar weight, R_i is the reaction source, and D_i^{eff} is the effective diffusion coefficient. The effective diffusion coefficient which

depends on the porosity ε and tortuosity τ can be calculated by the Knudsen diffusion ($D_{i,k}$) and molecular diffusion ($D_{i,j}$):

$$D_i^{eff} = \frac{\varepsilon D_{i,j} D_{i,k}}{\tau D_{i,j} + D_{i,k}} \quad (\text{Eq. 52})$$

The Knudsen diffusion is shown in Eq. 32, where \bar{r}_p is the averaged pore diameter.

$$D_{i,k} = 97 \bar{r}_p \left(\frac{T}{M_i} \right)^{\frac{1}{2}} \quad (\text{Eq. 53})$$

The molecular diffusion, which is shown in Eq. 33, is calculated by the Fuller equation.

$$D_{i,j} = \frac{1 \times 10^{-7} T^{1.75} \left(\frac{1}{M_i} + \frac{1}{M_j} \right)^{\frac{1}{2}}}{P \left(v_i^{1/3} + v_j^{1/3} \right)^{\frac{1}{2}}} \quad (\text{Eq. 54})$$

The expression of [19] is widely applied in the investigation of the relationship between porosity and tortuosity of particle modeling and behaviors, which is employed in this work, expressed as:

$$\tau = \frac{1}{\varepsilon} \quad (\text{Eq. 55})$$

The change of porosity ε is associated with the coke deposition rate, which can be described as below [11]:

$$\varepsilon = \varepsilon_0 - \frac{r_c M_c}{\rho_c} \Delta t \quad (\text{Eq. 56})$$

Where ϵ_0 is the initial porosity, ρ_c is the and M_c is the molar weight of coke.

3.3.1.2 Reaction kinetic model

The DRM and CH₄ decomposition reactions are shown in Eq. 37 and Eq. 38, respectively.



The rate expression in a Langmuir-Hinshelwood mechanism developed by Wang et al. (1999) [12] can be used to describe the DRM reaction as below:

$$r = \frac{k_1 P_{\text{CH}_4} P_{\text{CO}_2}}{(1 + K_1 P_{\text{CH}_4})(1 + K_2 P_{\text{CO}_2})} \quad (\text{Eq. 59})$$

Table 3 Kinetic parameters for the model of DRM reaction rate

Temp (C°)	$k_1 (\mu\text{mol}/g_{\text{cat}} \cdot \text{s} \cdot \text{KPa}^2)$	$K_1 (\text{KPa}^{-1})$	$K_2 (\text{KPa}^{-1})$
500	0.20	0.00082	4.30
550	0.29	0.015	2.30
600	0.24	0.023	0.80
650	0.25	0.020	0.50
700	0.32	0.035	0.43

The corresponding reaction rate with the catalyst deactivation of CH₄ decomposition reaction developed by and Zavarukhin et al. (2004) [13], which is adopted to realize the coke deposition process in DRM is described as follows:

$$r = a \cdot r_c \max \quad (\text{Eq. 60})$$

$$r_c \max = k \frac{p_{CH_4} - p_{H_2}/K_p}{(1 + k_H \sqrt{p_{H_2}})^2} \quad (\text{Eq. 61})$$

$$k = \exp \left(20.492 - \frac{104200}{RT} \right) \quad (\text{Eq. 62})$$

$$K_p = 5.088 \times 10^5 \exp \left(- \frac{91200}{RT} \right) \quad (\text{Eq. 63})$$

$$k_H = \exp \left(\frac{163200}{RT} - 22.426 \right) \quad (\text{Eq. 64})$$

$$k_a = \exp \left(\frac{135600}{RT} - 32.077 \right) \quad (\text{Eq. 65})$$

Where r_c is the rate of coke production. C is the specific coke content on the catalyst, depending on time, temperature, partial pressures of methane, p_{CH_4} , and hydrogen, p_{H_2} , and the type of catalyst. a is relative catalyst activity. k_H and K_p are the equilibrium constants. k and k_a are specific rate constant and deactivation rate constant, respectively.

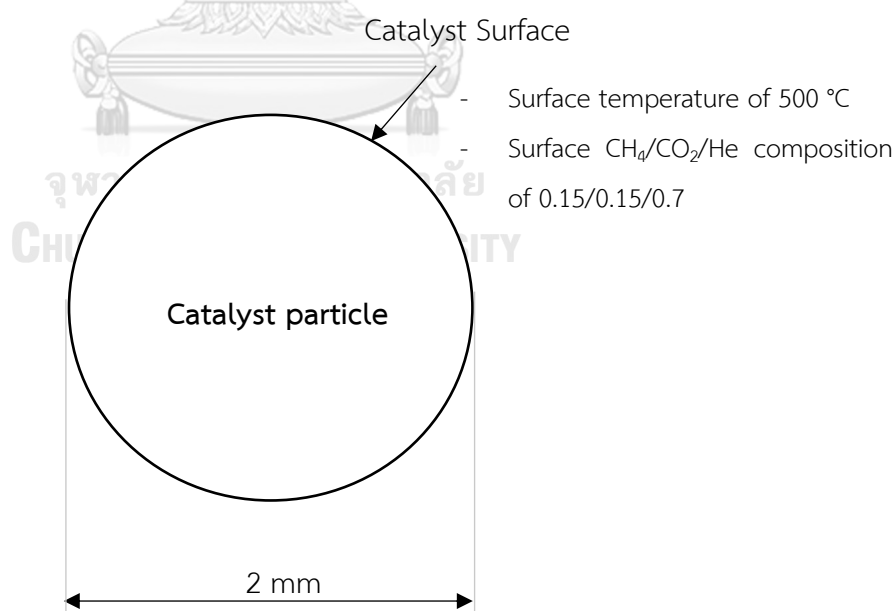
3.3.2 System description and boundary condition

A Three-dimensional (3D) unsteady-state model was carried out to study coke formation behavior over a single Ni/Al₂O₃ catalyst particle for the DRM process. Fig. 4 has shown a schematic of a sphere single catalyst particle geometry domain. The sphere particle shape with a particle diameter of 2 mm and particle pore diameter of 15 nm was used. The density and initial porosity of the particle are 1974 kg³/m and 0.45, respectively. Fig. 4 shows a schematic of a sphere single catalyst particle geometry domain.

As the initial condition, the single-phase gas composition at the surface with the specified concentration temperature and pressure was fed into the particle from the particle's surface in every direction which is perpendicular to the particle surface. The model was assumed to have no external mass transfer limitation from bulk fluid to catalyst surface, so the species concentration and temperature can be set at the catalyst surface. Therefore, the CH₄/CO₂/He specie mole fractions were set as 0.15/0.15/0.7 with the catalyst surface temperature of 500 °C, while coke species were set as a zero-mass flux condition. The detailed operating parameters and physical properties are listed in Table 4. The commercial software ANSYS-FLUENT 2020R1 is used to solve the equations.

Table 4 Operating conditions and physical properties used in the simulation.

Parameters	Value
Particle diameter (mm)	2
Particle density (kg ³ /m)	1974
Coke density (kg ³ /m)	2360
Particle pore diameter (nm)	15
Particle initial porosity (-)	0.45
Particle volume (mm ³)	4.19
Gas composition at surface (CH ₄ /CO ₂ /He) (-)	0.15/0.15/0.7
Catalyst surface temperature (°C)	500
Initial pressure inside catalyst (MPa)	0.1

**Figure 4** A schematic of a sphere single catalyst particle geometry domain.

3.3.3 Assumptions

The assumptions of calculation for coke formation behaviors from the DRM process over the Ni/Al₂O₃ catalyst can be listed as below:

1. This work predicts atomic coke formation over a sphere alumina-supported nickel catalyst (Ni/Al₂O₃) particle for dry reforming of methane (DRM)
2. The used kinetic model was assumed there is no mass transfer limitation
3. The model was assumed that the deactivation of catalyst is only caused by coke formation which blocks porosity on a catalyst particle.
4. The change of porosity is implemented by the change of coke volume deposition on the pore structure inside the catalyst particle
5. The model was assumed to have no external mass transfer limitation from bulk fluid to catalyst surface, so the species concentration and temperature can be set at the catalyst surface.

3.4 Study the effect of operating parameters on coke formation for the DRM reaction

The effect of operating parameters on coke formation behavior over a single Ni/Al₂O₃ catalyst particle for the DRM process was studied by varied CH₄/CO₂ ratio and reaction temperatures. The effect of reaction temperature of 500, 550, and 600 was studied. The CH₄/CO₂ ratio was performed with a feed composition of 0.15/0.15, 0.15/0.075, and 0.075/0.15. A balance gas of He was adjusted to maintain a total absolute pressure of 0.1 MPa.

CHAPTER IV

RESULTS AND DISCUSSION

4.1 Grid independence test

Four different sets of grid numbers consisting of 290,265, 222,953, 176,479, 114,488 elements were studied. The detail of quantity and quality are listed in Table 5.

Table 5 Grid quantity and quality for different grid size

Grid quantity		Grid quality		Size (mm)
Cells	Nodes	Minimum Orthogonal	Maximum skewness	
290,965	107,675	0.20158	0.79842	0.040
222,953	83,808	0.18618	0.79967	0.045
176,479	67,522	0.16235	0.79187	0.050
114,488	44,949	0.17243	0.79343	0.060

The distributions of the specific coke accumulation on the catalyst particle for four sets of computational grids were compared as shown in Fig. 5. The results show that the mesh with 222,953 elements provides an accurate result for the values of specific coke accumulation with the maximum relative error of 4 percent compared to the final mesh. Therefore, according to the grid independence test, further models would be generated with the grid number of 222,953 with a maximum element size of 0.045 mm.

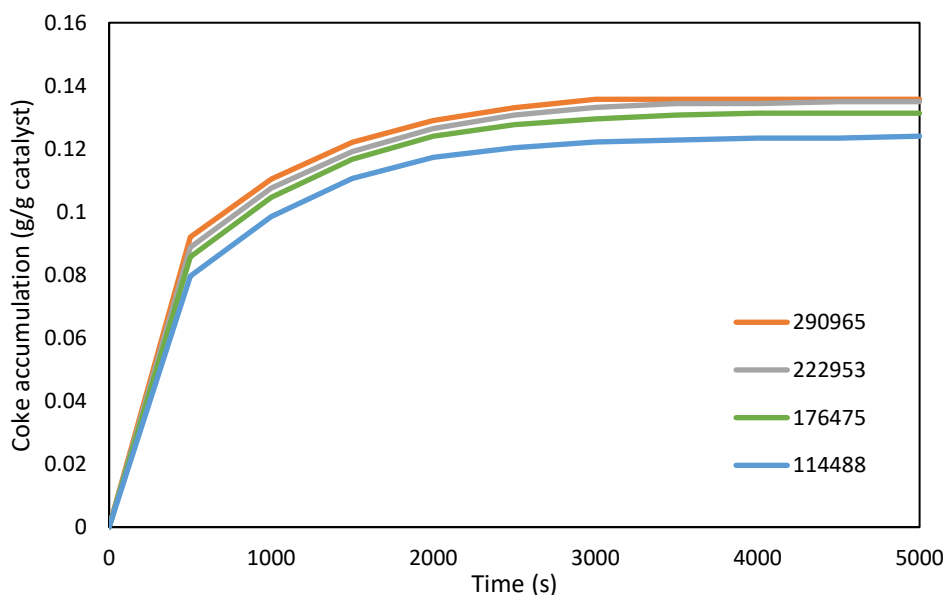


Figure 5 Distribution of the specific coke accumulation on the catalyst particle for four sets of computational grids.

4.2 Model validation using methane cracking reaction

4.2.1 Model validation using deactivation rate

In order to validate the model, the simulation results were compared with the data reported by Yang et al. (2021) [14]. The simulation results and data from Yang et al. (2021) of time dependencies of the specific coke accumulation and reaction rate on the catalyst particle are shown in Fig. 6 and Fig. 7, respectively. The coke content rises with the increase of time and reaches the maximum coke content of 0.136 g/g catalyst at 2500 seconds reaction time. Moreover, it can be seen that the simulation results are in good agreement with the experimental data, and the difference between the maximum coke content from simulation and yang et al. (2021) results is not more than 5 percent. Fig 8 and Fig. 9 show the simulation results of the activity and porosity on the catalyst particle, respectively. The comparison of data points from Yang et al. (2021) is well approximated and fitted the same curve which is obtained from the simulation results.

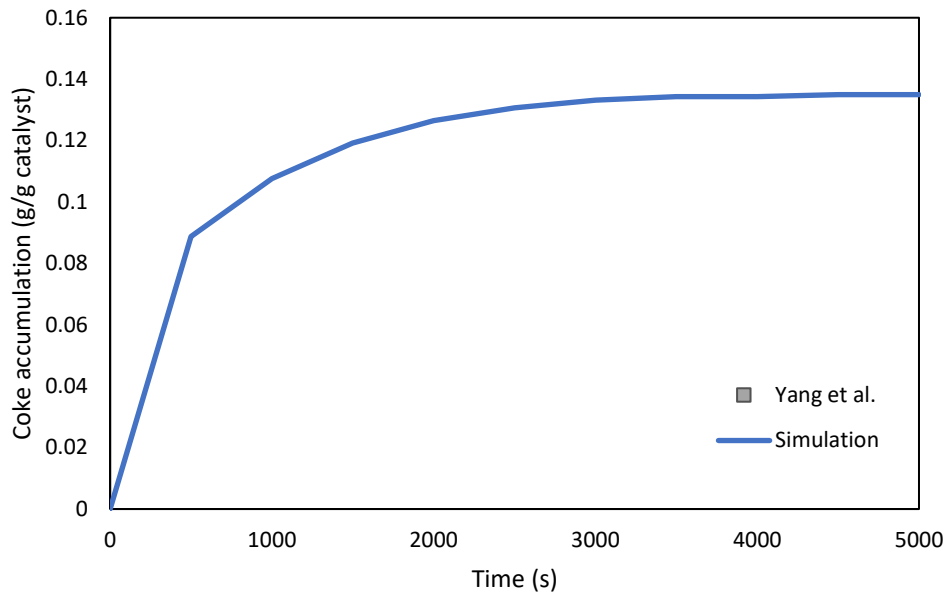


Figure 6 Yang et al. (points) and simulation (lines) time dependencies of specific coke accumulation on the catalyst particle.

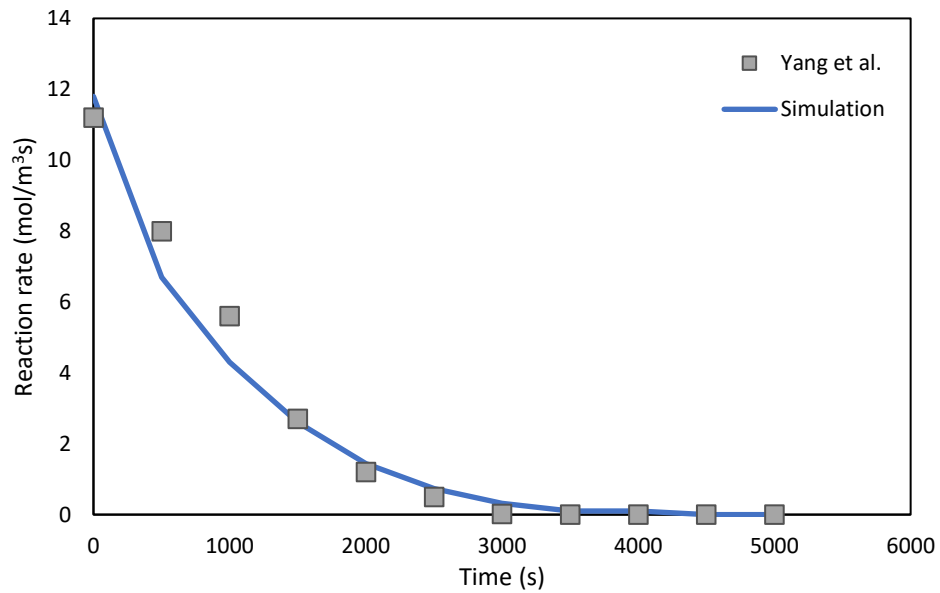


Figure 7 Yang et al. (points) and simulation (lines) time dependencies of reaction rate on the catalyst particle.

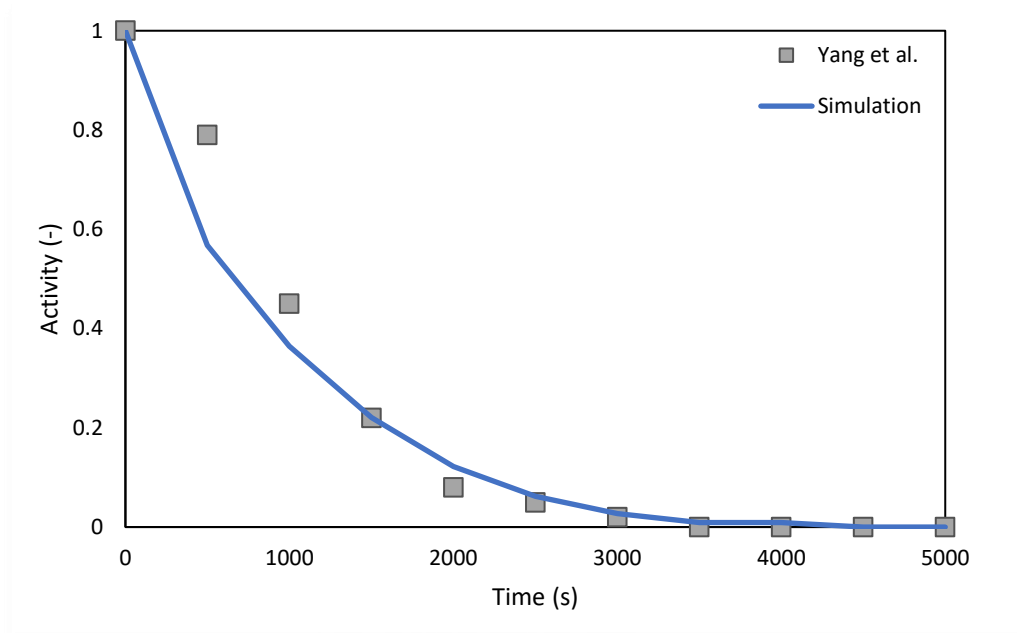


Figure 8 Yang et al. (points) and simulation (lines) time dependencies of activity on the catalyst particle.

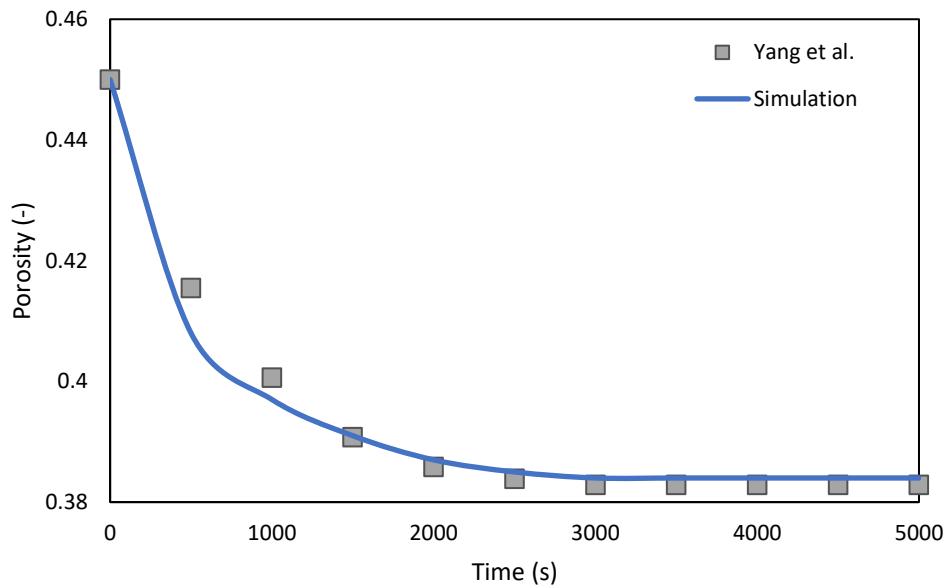


Figure 9 Yang et al. (points) and simulation (lines) time dependencies of porosity on the catalyst particle.

The model validation shows that the results obtained by simulation results are precise and can be used as a prototype for system design and modification. The further study is to apply the relation of porosity change caused by coke formation instead of deactivation rate.

4.2.2 Model validation using coke formation and porosity relation

4.2.2.1 Model validation

After model validation with the data reported by Yang et al. (2021), to apply the model to predict the coke formation on catalysts for DRM process without the activity equation. The change of porosity was used instead of the activity equation to study the effect of porosity change on coke formation. The suggested model was checked using experimental data reported by Zavarukhin et al. (2004) [13]. The distributions of reaction rate in a single catalyst particle with different H₂ content versus time are shown in Fig. 10.

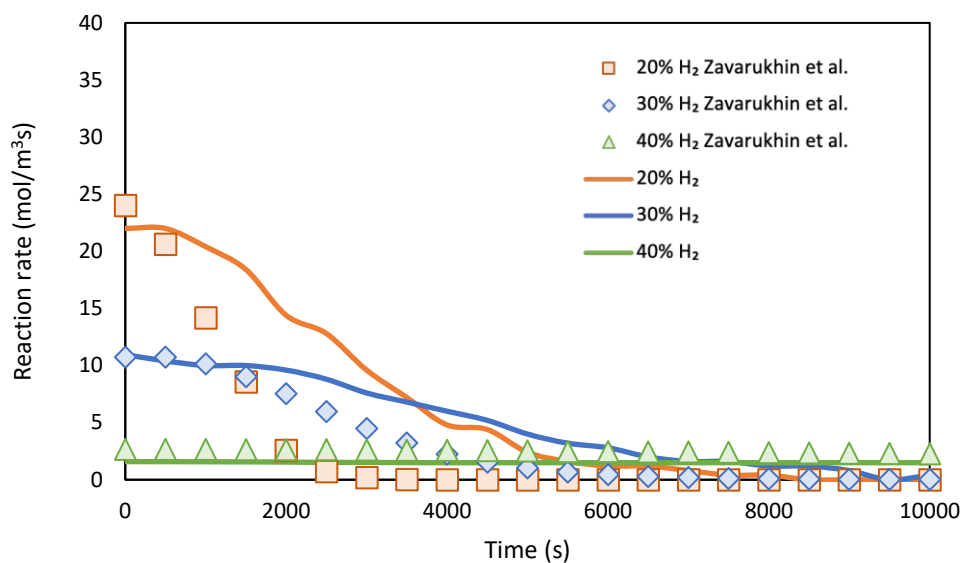


Figure 10 Zavarukhin et al. (points) and simulation (lines) time dependencies of reaction rate with different H₂ content on the catalyst particle.

The results show that the reaction rate of different H₂ content decrease with time as a result of carbon formation in a catalyst. By increasing the H₂ content, the reaction rate decrease. Additionally, 20% of H₂ content has the highest maximum reaction rate of coke formation which is estimated to be 23.70 mol/m³s as seen in Fig. 10. While the maximum reaction rate of 30% and 40% of H₂ content are 11.96 mol/m³s and 1.59 mol/m³s, respectively.

Fig. 11 shows the distributions of reaction rate in a single catalyst particle with the different temperatures at 40% H₂ content versus time. The results show that the reaction rate increases by the enhancement of temperature due to the endothermic nature of the CH₄ decomposition reaction.

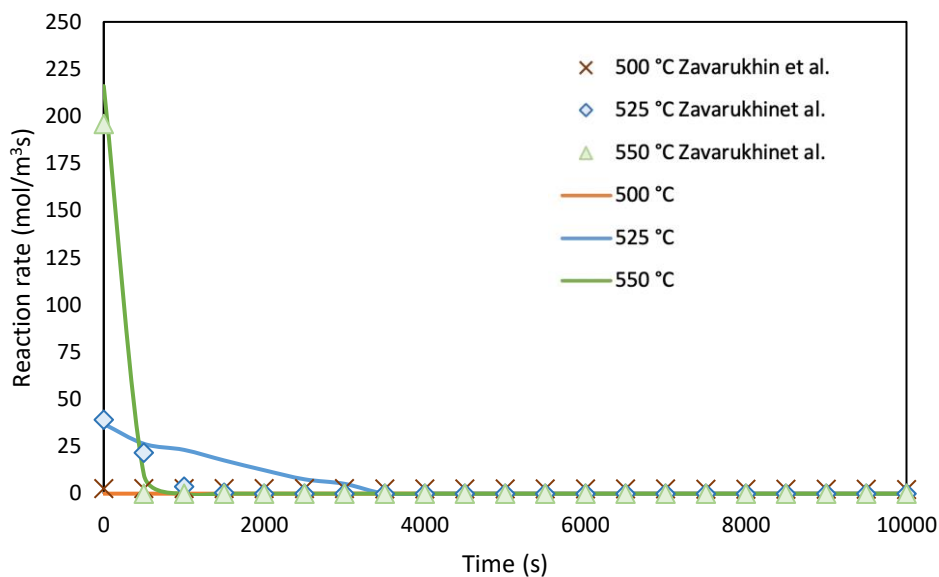


Figure 11 Zavarukhin et al. (points) and simulation (lines) time dependencies of reaction rate with the different temperature at 40% H₂ content on the catalyst particle.

When comparing the simulation results and experimental data, the simulation results obtained from Fig 10 and Fig 11 show almost the same trend as the experimental data. Therefore, the model can be used to predict coke formation in the DRM process.

Moreover, time dependencies of porosity and effective diffusion coefficient with different H₂ content on the catalyst particle are obtained from the simulation shown in Fig 12 and 13, respectively. The results show that the catalyst porosity and effective diffusion coefficient of different H₂ content decrease with time as a result of coke formation in a catalyst. In comparison to the other values of H₂ content, the porosity and effective diffusion coefficient of 20% of H₂ content have the lowest due to the highest maximum reaction rate of coke formation. Therefore, coke formation has a direct impact on porosity and effective diffusion coefficient. By increasing the

H₂ content, the coke accumulation in the catalyst particle decreased and eventually increased porosity and effective diffusion coefficient.

The radius distribution of coke concentration with 20% H₂ content inside the catalyst particle at the different reaction times is shown in Fig. 14-16. Fig. 17 shows the instantaneous contour of coke accumulation with 20% H₂ content on the catalyst particle. It can be observed that the coke concentration is initially formed near the particle surface. As the reaction progressed, the coke concentration appears in the whole particle as seen in Fig. 17c.

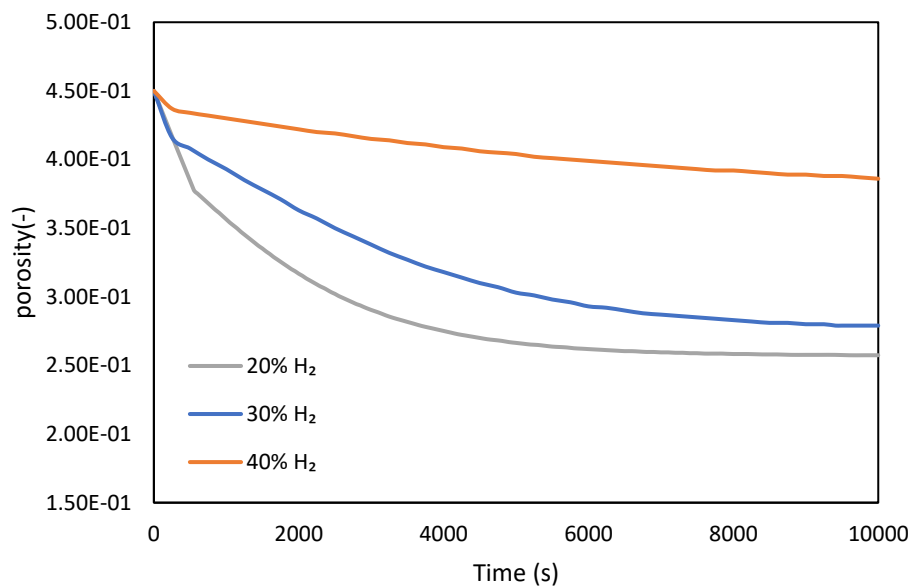


Figure 12 Time dependencies of porosity with different H₂ content on the catalyst particle.

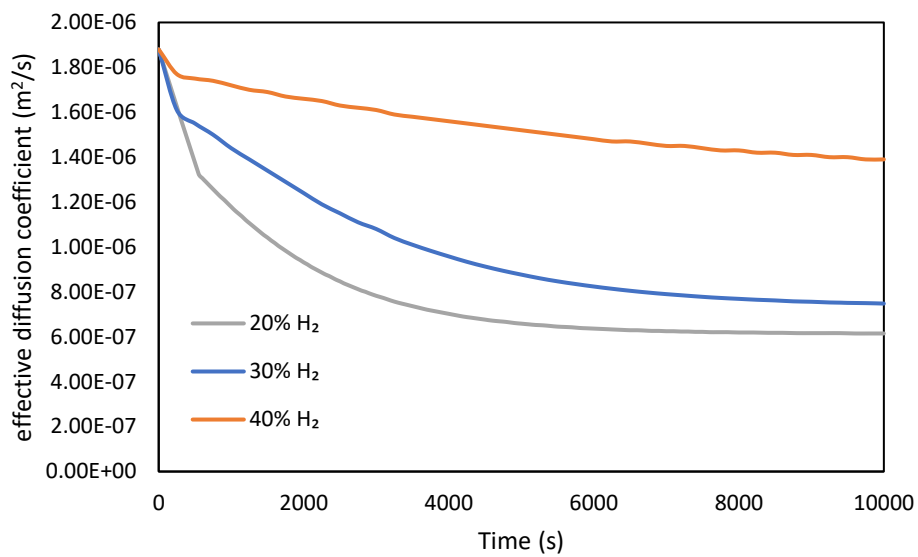


Figure 13 Time dependencies of effective diffusion coefficient with different H₂ content on the catalyst particle.

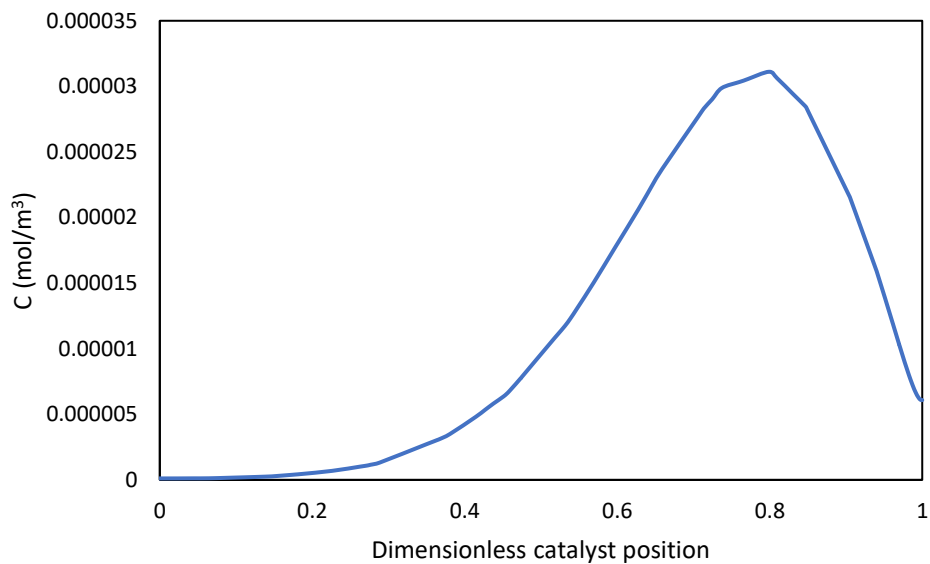


Figure 14 Radius distribution of coke concentration with 20% H₂ content on the catalyst particle at 4 sec.

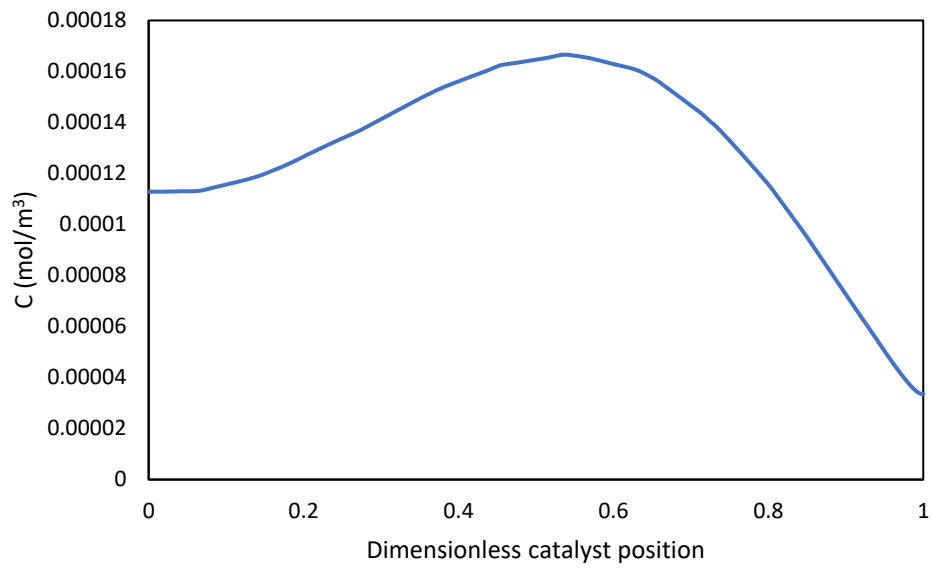


Figure 15 Radius distribution of coke concentration with 20% H₂ content on the catalyst particle at 20 sec.

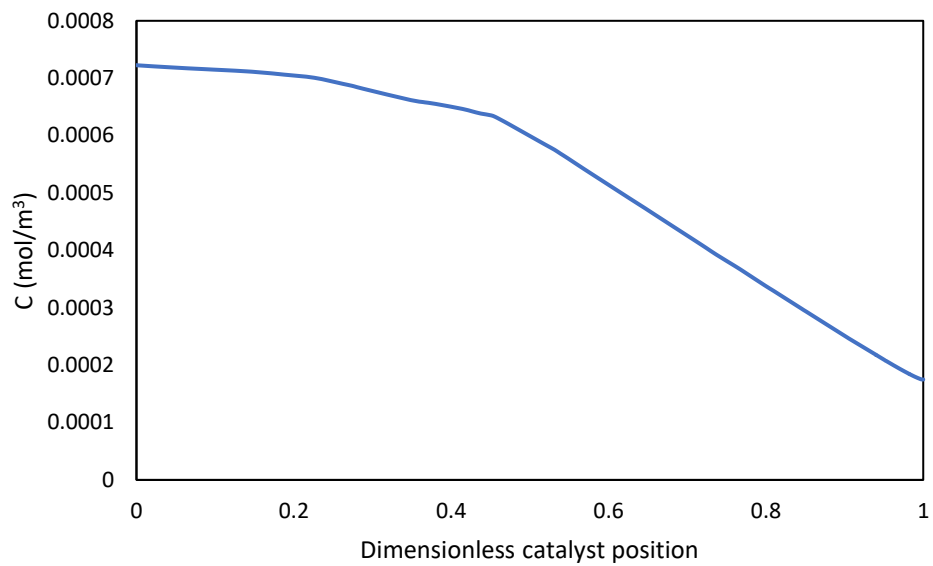


Figure 16 Radius distribution of coke concentration with 20% H₂ content on the catalyst particle at 2000 sec.

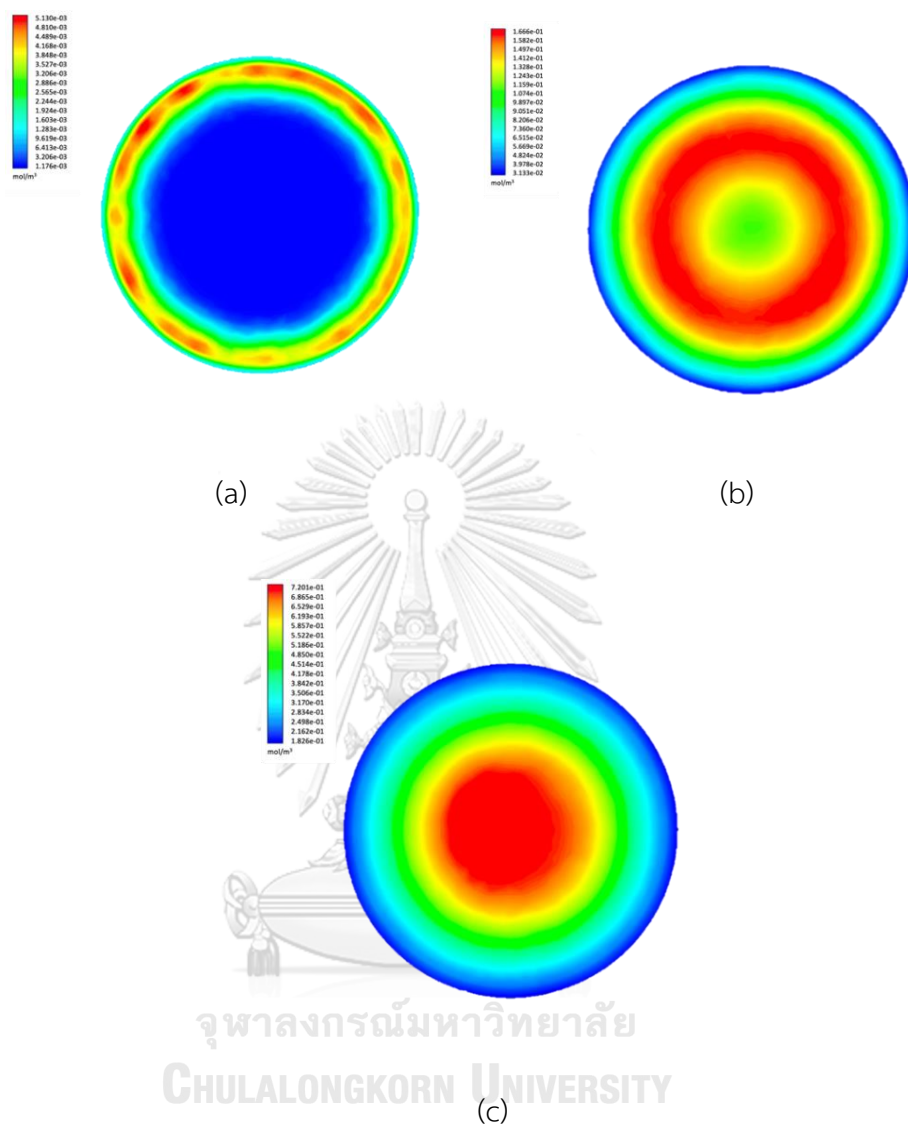


Figure 17 The instantaneous contour of coke accumulation with 20% H_2 content on the catalyst particle at (a) 4 sec (b) 20 sec (c) 2000 sec.

4.2.2.2 Model optimization

When the reaction rate between Zavarukhin et al. (2004) data and simulation results are compared, it shows that the reaction rates obtained from the simulation results by varying H₂ content and temperature from Fig 10 and Fig.11, respectively show almost the same trend with the experimental data. However, the reaction rate obtained from the simulation results decreased slower than experimental data with the maximum mean absolute error of 6.83 compared to the experimental data. The reason for the discrepancy between simulation and experiments is due to in experiment the deactivation of catalyst is not only caused by coke formation which blocks pores and active sites in catalyst but there are many factors for deactivation of catalyst in the experiment. For example, a catalyst solid may be poisoned by any contaminants present in the feed. Thermal degradation of catalysts results from loss of support area due to support collapse and of catalytic surface area due to pore collapse on crystallites of the active phase. Abrasion results in the loss of catalytic material; loss of internal surface area due to the mechanical-induced crushing of the catalyst particle [20]. All these example factors can lead to a faster decrease of reaction rate in the experiment.

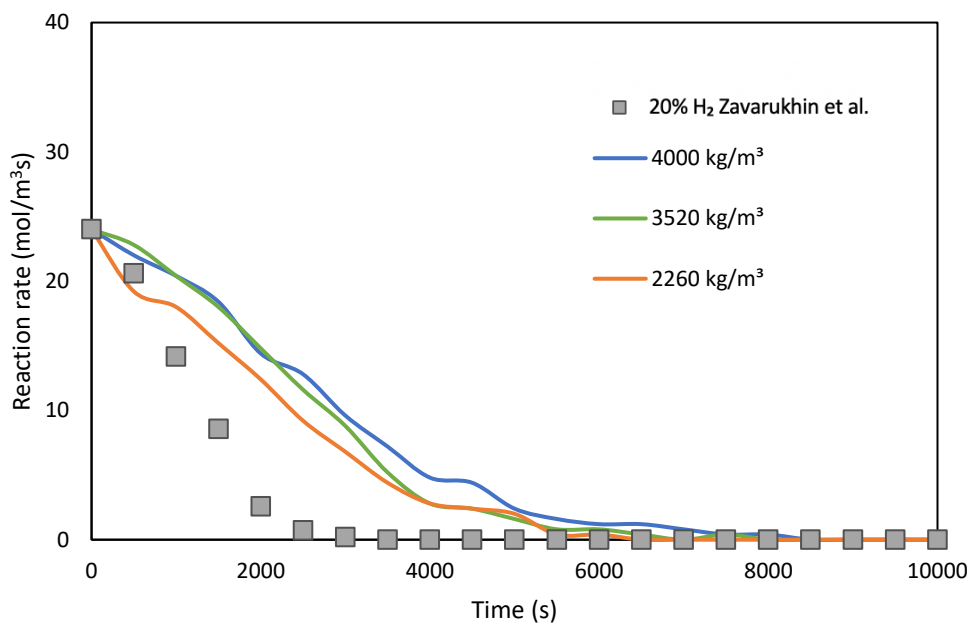


Figure 18 Zavarukhin et al. (points) and simulation (lines) time dependencies of reaction rate with different coke density at 20% H₂ content and pore size of 15 nm on the catalyst particle.

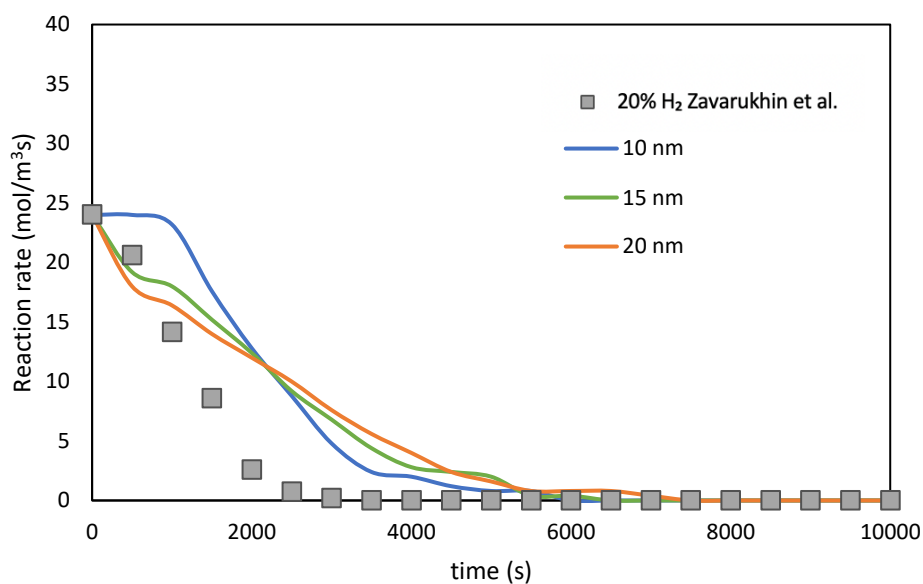


Figure 19 Zavarukhin et al. (points) and simulation (lines) time dependencies of reaction rate with different catalyst pore size at 20% H₂ content and coke density of 2.36 kg/m³ on the catalyst particle.

To adjust the simulation model to be more accurate, the adjusted variables such as coke density and particle pore size were studied. Coke density and particle pore size are variables associated with the change of porosity and mass diffusion in catalysts described in Eq.31 and Eq. 34. In this model, it is assumed that the coke formation in catalyst particles is started to form from atomic carbon, which has a density of 2.36 kg/m^3 . Thus, the coke density can be varied in a range of more than 2.36 kg/m^3 depending on the carbon structure formation in the catalyst. Fig.18 shows time dependencies of reaction rate with different coke densities at 20% H_2 content and pore size 15 nm on the catalyst particle.

The results show that by decreasing the coke density, the reaction rate shifts down and decreases faster. The common particle pore size for $\text{Ni/Al}_2\text{O}_3$ is in the range of 5-20 nm depending on the methods of catalyst preparation [21]. Fig.19 shows time dependencies of reaction rate with different pore sizes at 20% H_2 content and coke density of 2.36 kg/m^3 on the catalyst particle. The decrease in pore size leads to and decrease in the mass diffusion described in Eq.32. In comparison to the other two values of pore size, the reaction rate of 10 nm decreases slowest during 2000 seconds. While the reaction rates obtained from pore sizes of 15 and 20 nm are in the same trend. Therefore, the coke density of 2.36 kg/m^3 and particle pore size 15 nm were used in the simulation for the prediction of coke formation behaviors inside catalyst for DRM process.

4.3 Coke formation behavior for dry reforming of methane reaction in a catalyst particle

After model validation with the CH_4 decomposition reaction, the result obtained from the simulation results show good agreement with the experimental data. The optimized model was used further to study the coke formation behavior for the DRM process. This section is divided into two parts which are: (i) study the concentration profile and coke formation in the $\text{Ni}/\text{Al}_2\text{O}_3$ Catalyst for DRM reaction and (ii) study the effect of operating parameters on coke formation and concentration profile for the DRM reaction

4.3.1 Concentration profile and coke formation

4.3.1.1 CO and H_2 concentration

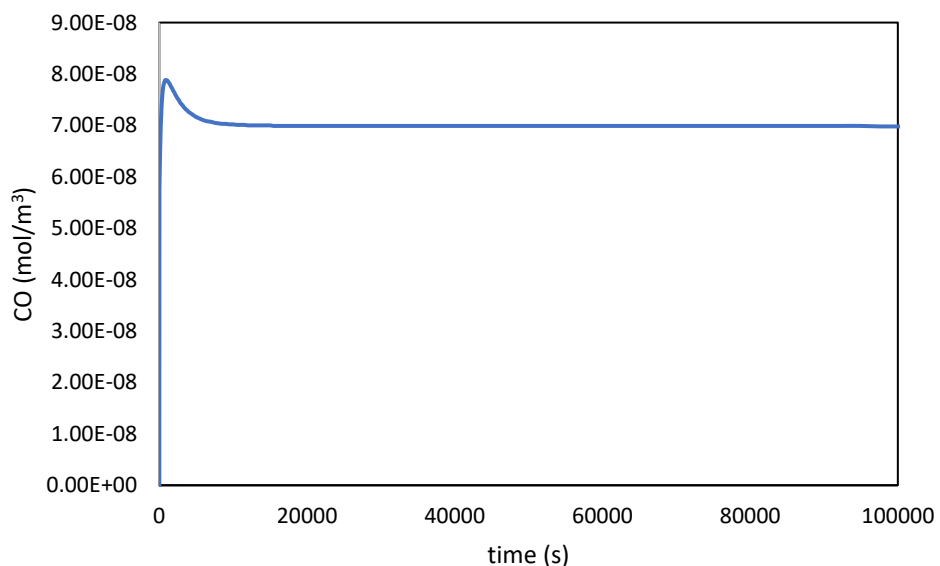


Figure 20 Time dependencies of CO concentration on the catalyst particle for DRM.

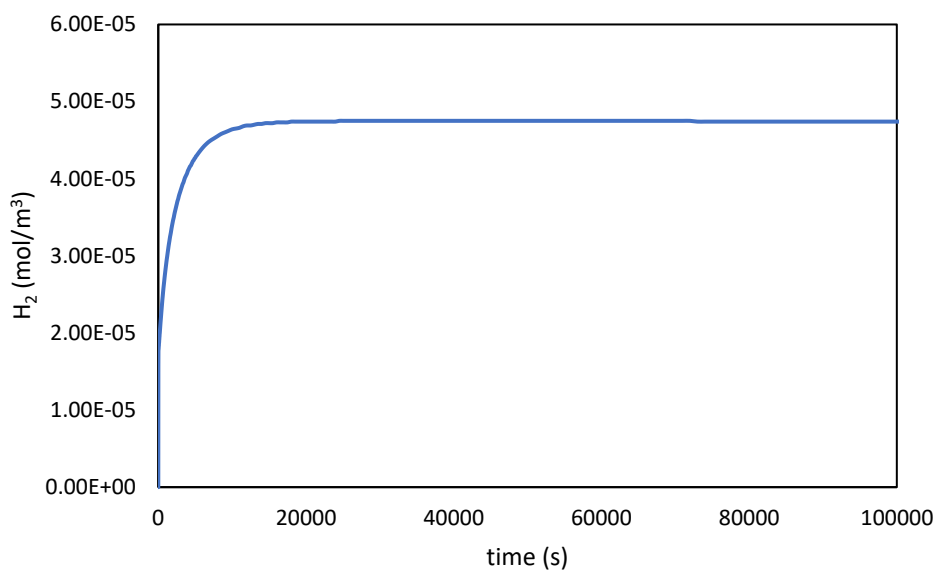


Figure 21 Time dependencies of H₂ concentration on the catalyst particle for DRM.

CO and H₂ concentration in a single particle of Ni/Al₂O₃ catalyst versus time are shown in Fig. 20 and 21, respectively. Both H₂ and CO concentrations increase with the increasing reaction time. At the start stage, CO concentration produced from the DRM reaction has a slight decrease due to gas species products that are produced from the reaction can diffuse out from the catalyst particle. The CO concentration produced from the DRM process is estimated to be 6.98×10^{-8} mol/m³ and remains constant after 6000 seconds of reaction time while H₂ concentration produced from DRM and CH₄ decomposition process is 4.74×10^{-5} mol/m³ and reach this value at 18500 seconds.

The instantaneous contours of CO and H₂ concentration versus time inside a single particle of Ni/Al₂O₃ catalyst are displayed in Fig. 22 and 23, respectively. It can be observed that the H₂ and CO concentration is initially formed near the particle surface. As the reaction progressed, the CO and H₂ concentration appears in the whole particle as seen in Fig. 22c and Fig. 23c, respectively. These results are in agreement with those of Yang et al (2021) [22] which reported the instantaneous contours of H₂ concentration on a catalyst particle.

When the CO and H₂ concentrations are compared, it is clear that the CH₄ decomposition reaction is easier reactive than the DRM reaction. This is due to the activation energy for CO production being higher than that for either CH₄ or CO₂ consumption. The activation energy for CO production was about 90.0 KJ/mol, while activation energy for CO₂ and CH₄ are 56.1 KJ/mol and 50.9 KJ/mol, respectively [23]. The catalytic reaction of DRM involves the first chemisorption of CH₄ and CO₂ on active sites. The lower activation energies for CH₄ and CO₂ consumption could indicate that the chemisorption stages for the two reactants are easier, while CO production is more difficult.



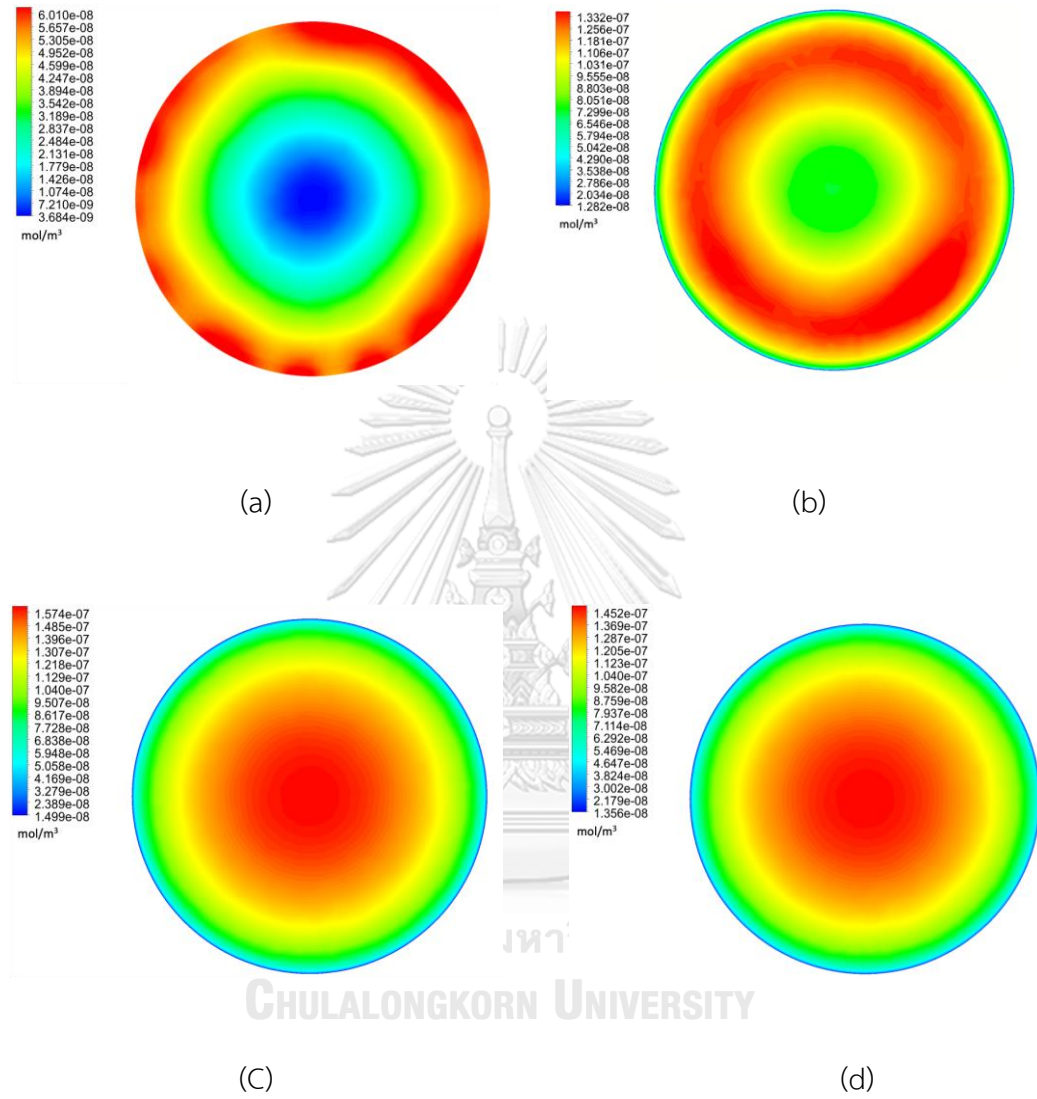


Figure 22 The instantaneous contour of CO concentration inside the particle at (a) 20 sec (b) 200 sec (c) 2000 sec (d) 10000 sec.

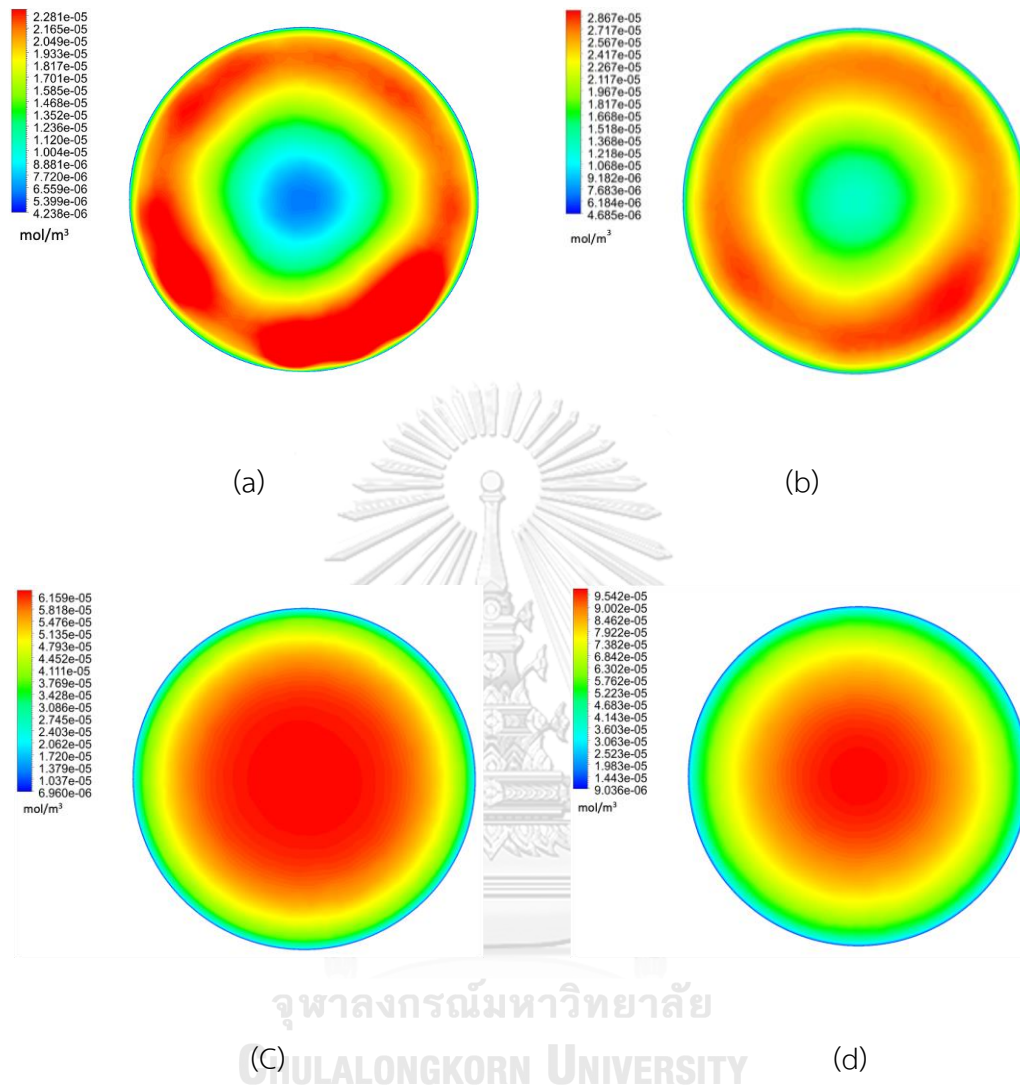


Figure 23 The instantaneous contour of H_2 concentration inside the particle at (a) 20 sec (b) 200 sec (c) 2000 sec (d) 10000 sec.

4.3.1.2 Coke accumulation

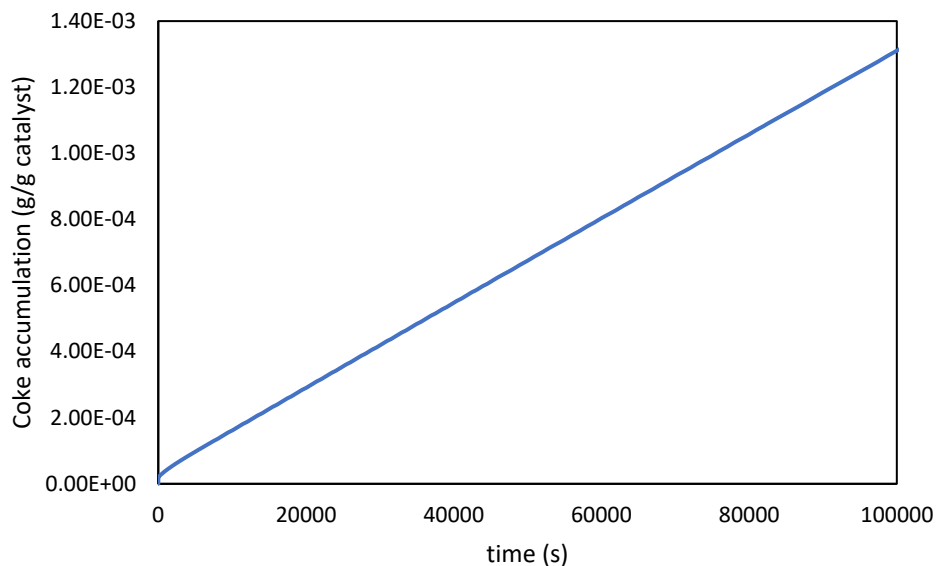


Figure 24 Time dependencies of coke accumulation on the catalyst particle for DRM.

The distribution of coke accumulation in a single particle of Ni/Al₂O₃ catalyst versus time is shown in Fig. 24. The coke accumulation inside the catalyst increases over time. In 100000 seconds of testing reaction time, the coke accumulation produced from the CH₄ decomposition reaction is estimated to be 1.31×10^{-3} g/g catalyst. The results show that the coke accumulation has a linear relation with reaction time. Voorhies et al (1945) [24] found a similar relation between carbon on catalyst versus reaction time.

The instantaneous contours of coke accumulation inside the particle are displayed in Fig. 25. Fig. 26-28 shows the radius distribution of coke concentration inside the catalyst particle at the different reaction times. It can be observed that the coke formation was initially formed at the surface of the catalyst and gradually formed at the center. As the reaction progressed, the coke formation in the center

becomes more substantial. The coke formation appears in the whole particle as seen in Fig. 25c and Fig. 25d.

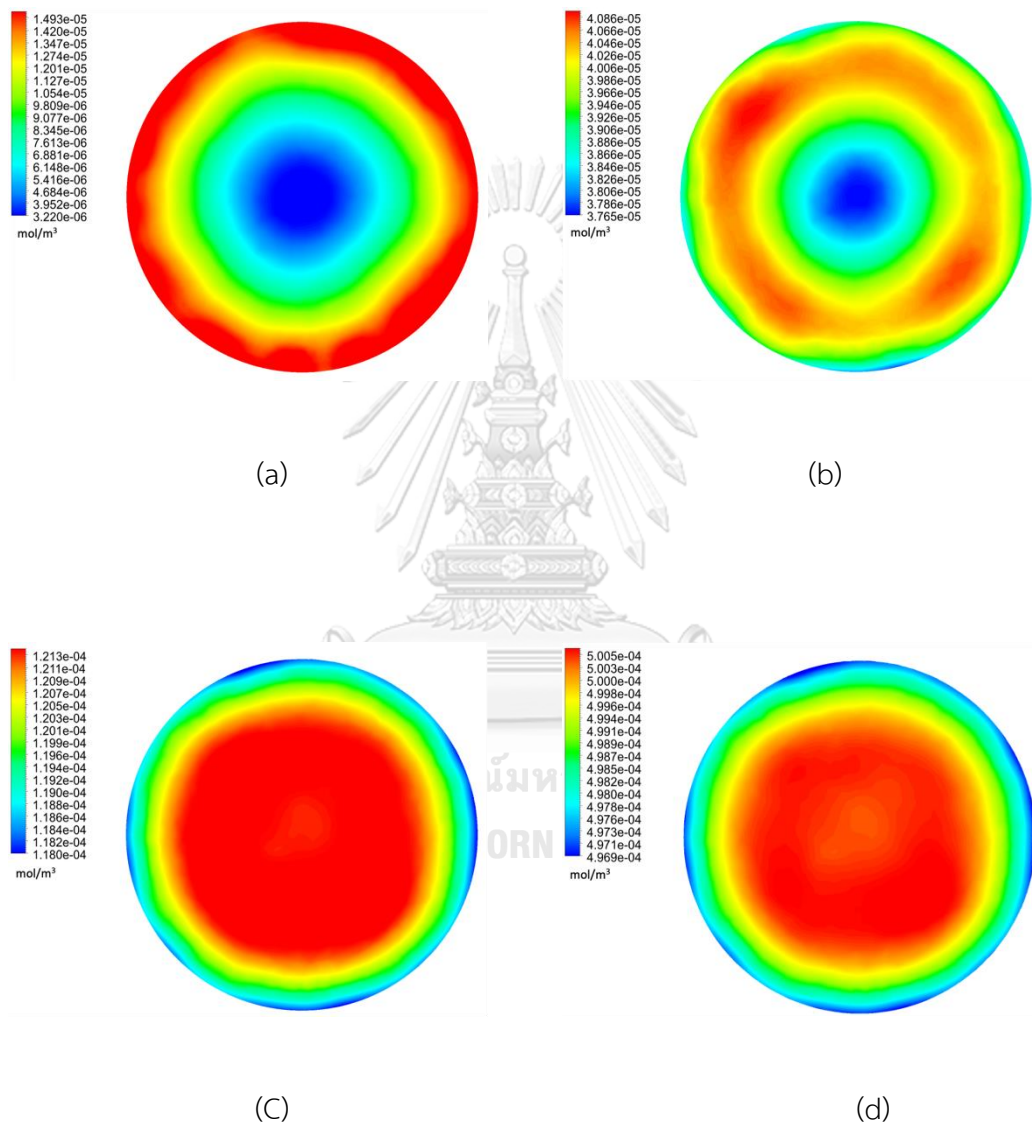


Figure 25 The instantaneous contour of coke accumulation inside the particle at (a) 20 sec (b) 2000 sec (c) 10000 sec (d) 50000 sec.

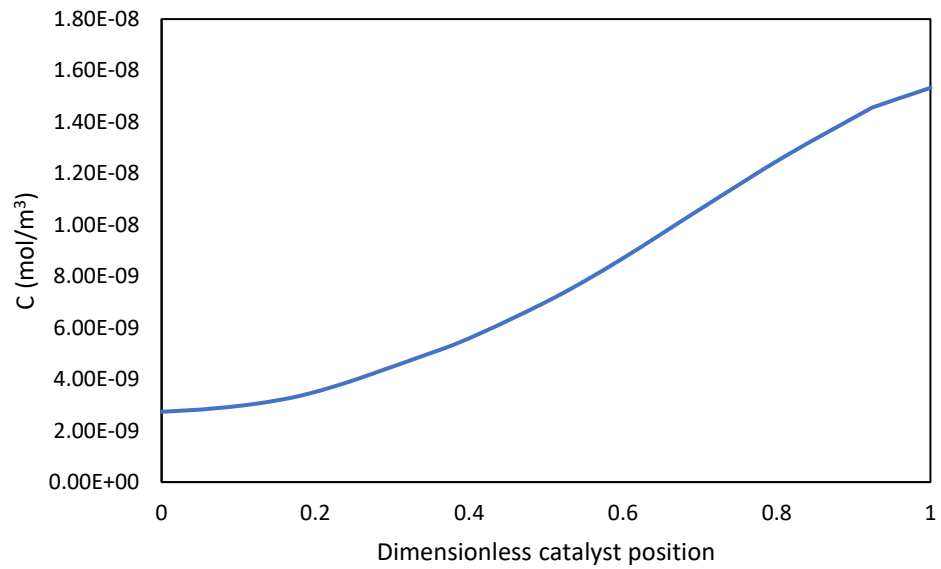


Figure 26 Radius distribution of coke concentration on the catalyst particle for DRM
at 20 sec

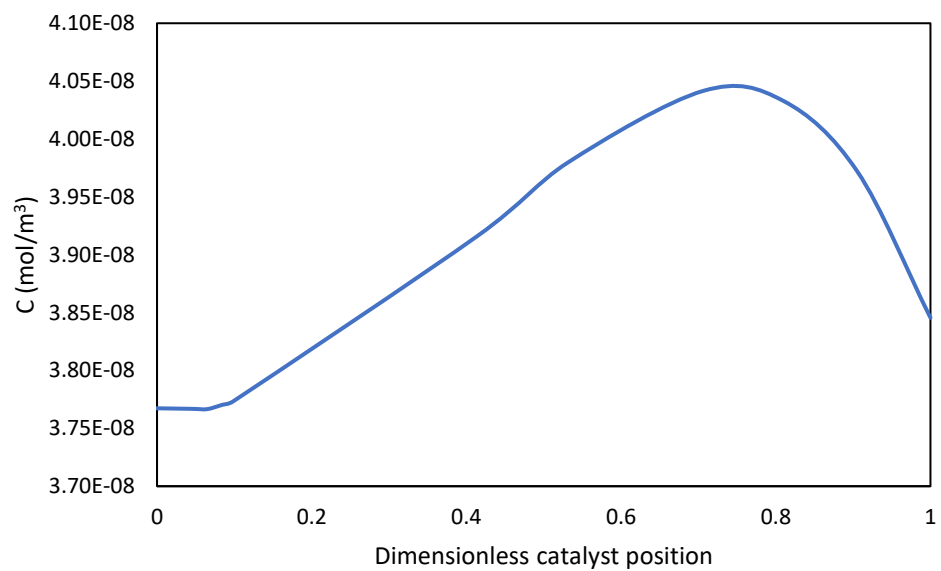


Figure 27 Radius distribution of coke concentration on the catalyst particle for DRM
at 2000 sec

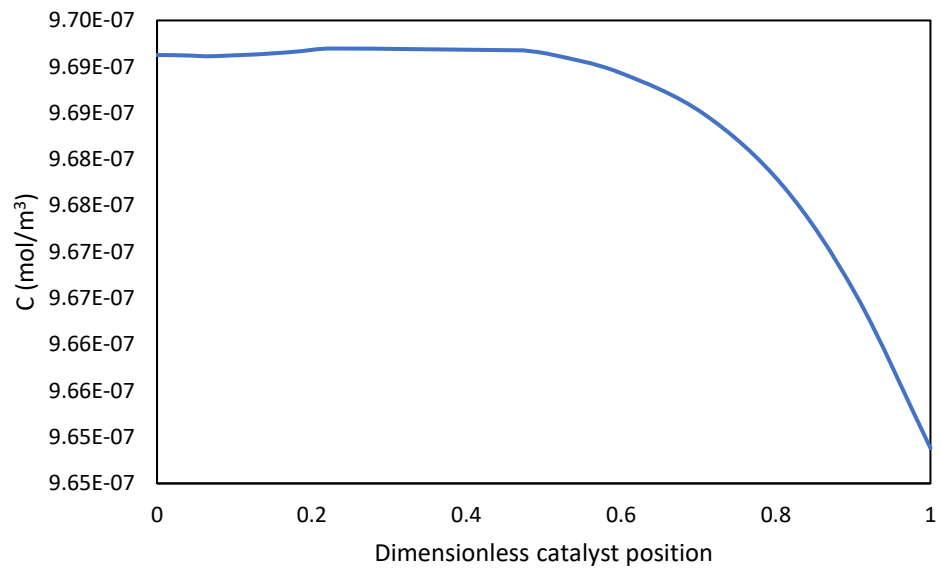


Figure 28 Radius distribution of coke concentration on the catalyst particle for DRM at 10000 sec

4.3.1.3 Porosity and effective diffusion coefficient

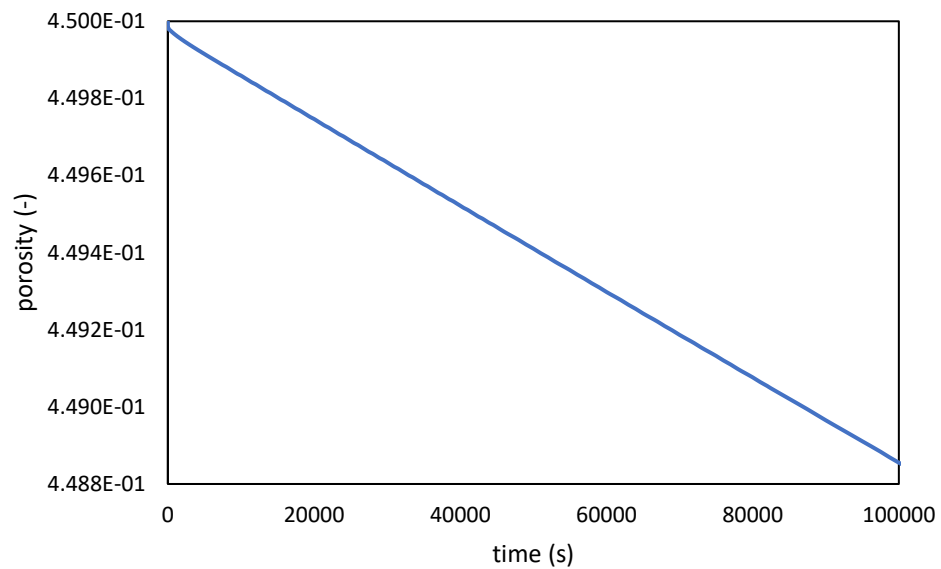


Figure 29 Time dependencies of porosity on the catalyst particle for DRM.

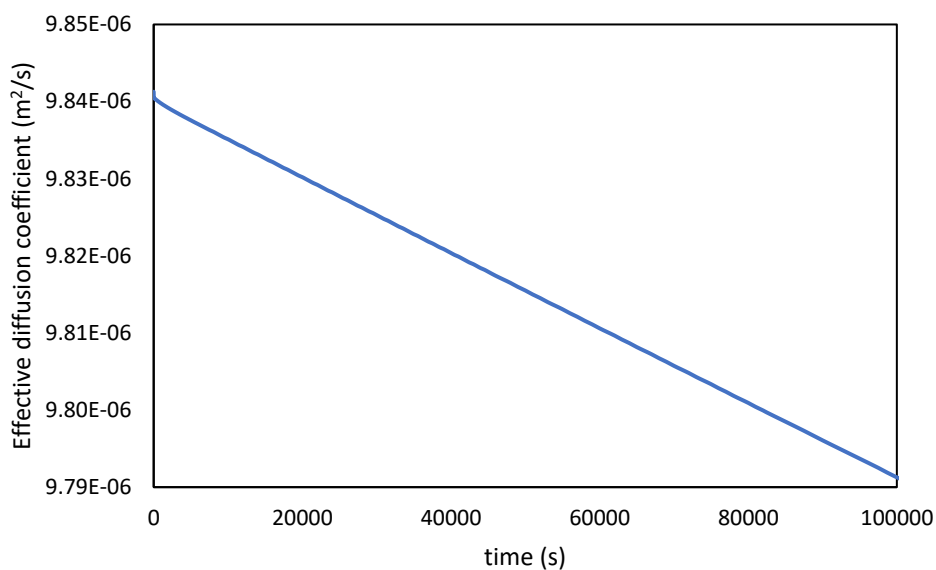


Figure 30 Time dependencies of effective diffusion coefficient on the catalyst particle for DRM.

The distribution and instantaneous contour of porosity versus time inside a single particle of Ni/Al₂O₃ catalyst are shown in Fig. 29 and Fig. 31, respectively. The results show that the porosity decreases with time due to the coke accumulation on catalyst particles. The porosity decreases from 0.4500 to 0.4489 at 100000 seconds reaction time.

Fig 33-35 show the radius distribution of porosity on the catalyst particle for DRM at the different reaction times. The results show that the profile and distribution of porosity inside the catalyst are reverse the profiles of coke accumulation. In the beginning, it can be observed that the porosity at the catalyst's center is higher than at the surface. As the reaction progressed, the coke formation in the center becomes more substantial, so the porosity near the surface is higher. Moreover, the carbon formation has an impact not only on the porosity but also on the internal diffusion process inside the catalyst.

The distribution and instantaneous contour of effective diffusion coefficient versus time inside the catalyst particle are shown in Fig. 30 and Fig. 32, respectively. It can be found that the diffusion coefficient decreases from $9.841 \times 10^{-6} \text{ m}^2/\text{s}$ to $9.791 \times 10^{-6} \text{ m}^2/\text{s}$ at 100000 seconds as a result of the decline of porosity inside the catalyst. Fig 3 6 -3 8 show the radius distribution of effective diffusion coefficient on the catalyst particle for DRM at the different reaction times. The results show that the effective diffusion coefficient profiles follow the same pattern as the porosity profile.



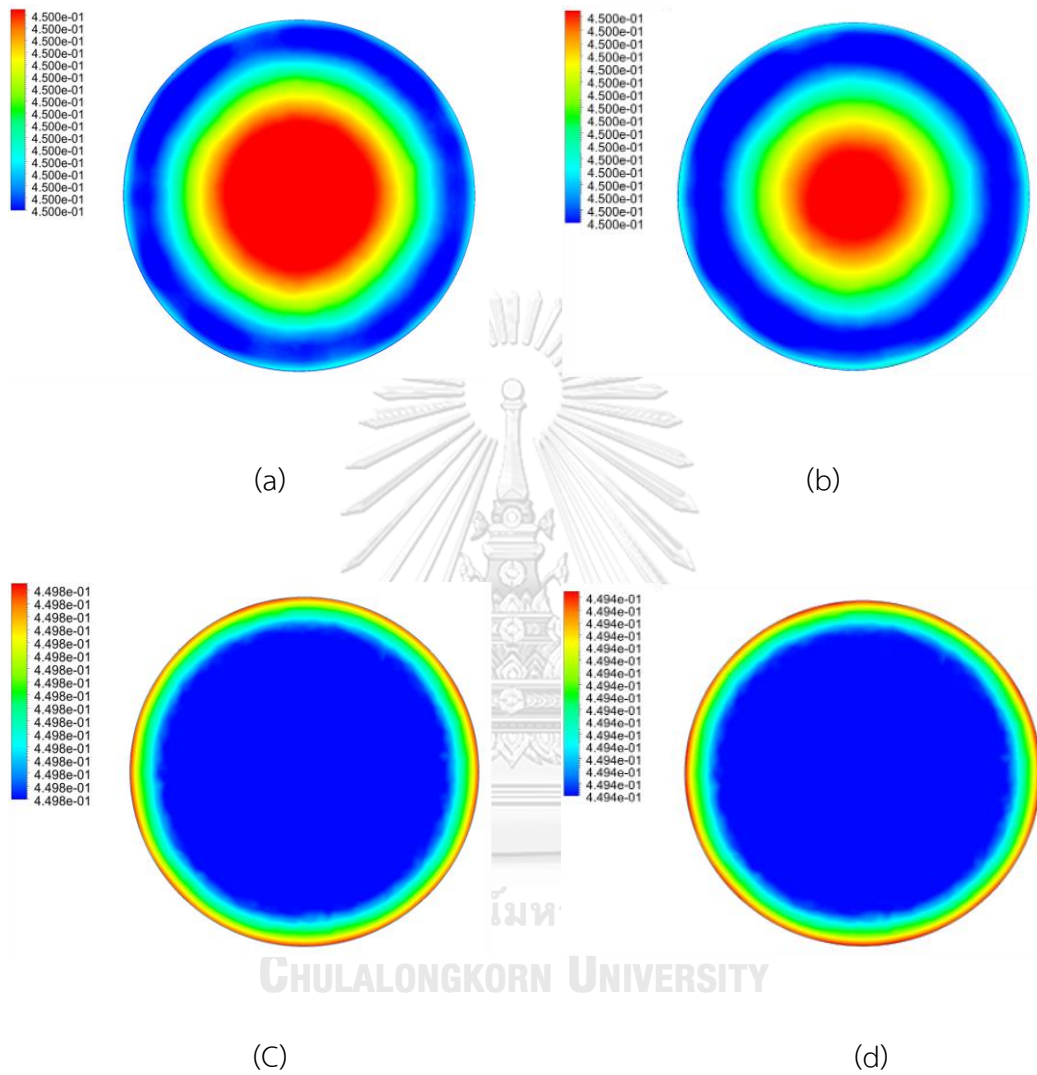


Figure 31 The instantaneous contour of porosity inside the particle at (a) 20 sec (b) 2000 sec (c) 10000 sec (d) 50000 sec.

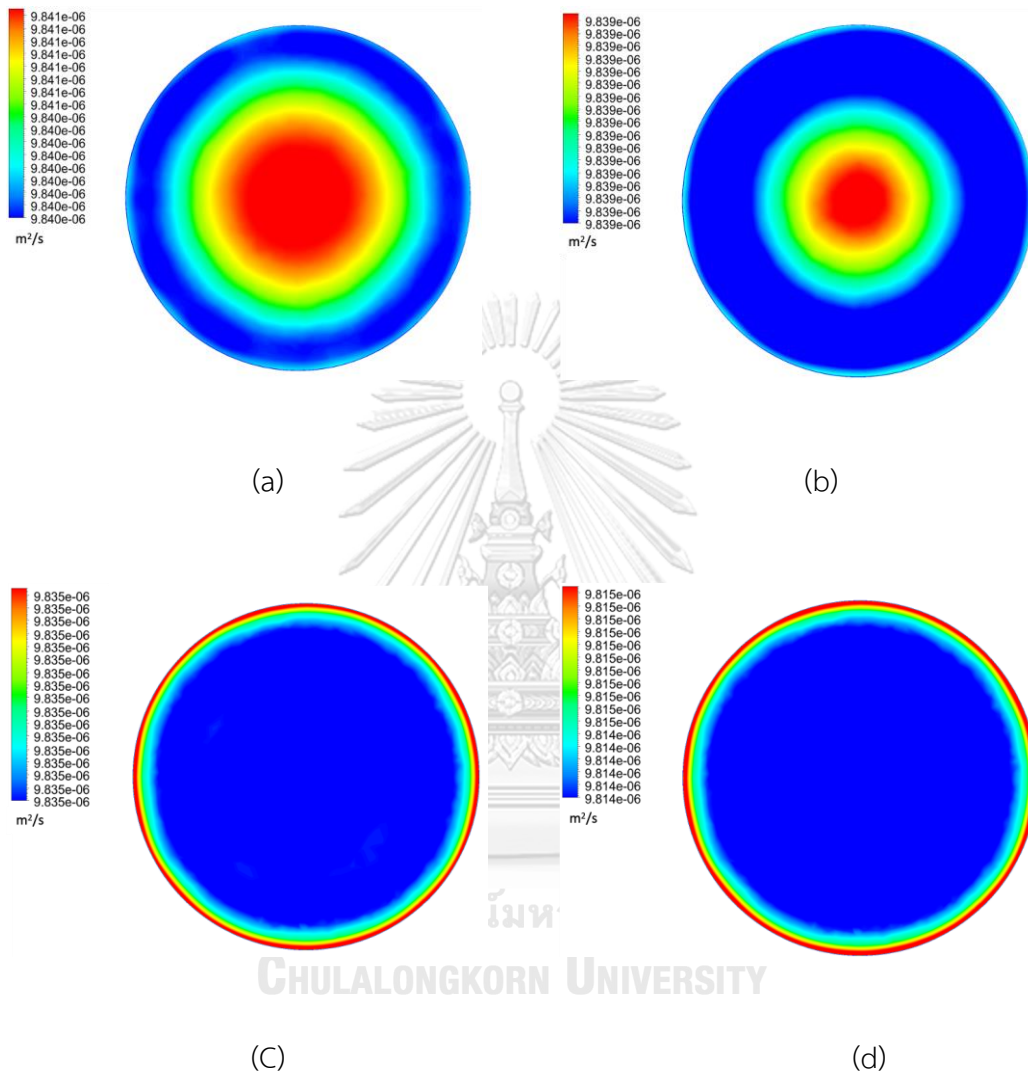


Figure 32 The instantaneous contour of effective diffusion coefficient inside the particle at (a) 20 sec (b) 2000 sec (c) 10000 sec (d) 50000 sec.

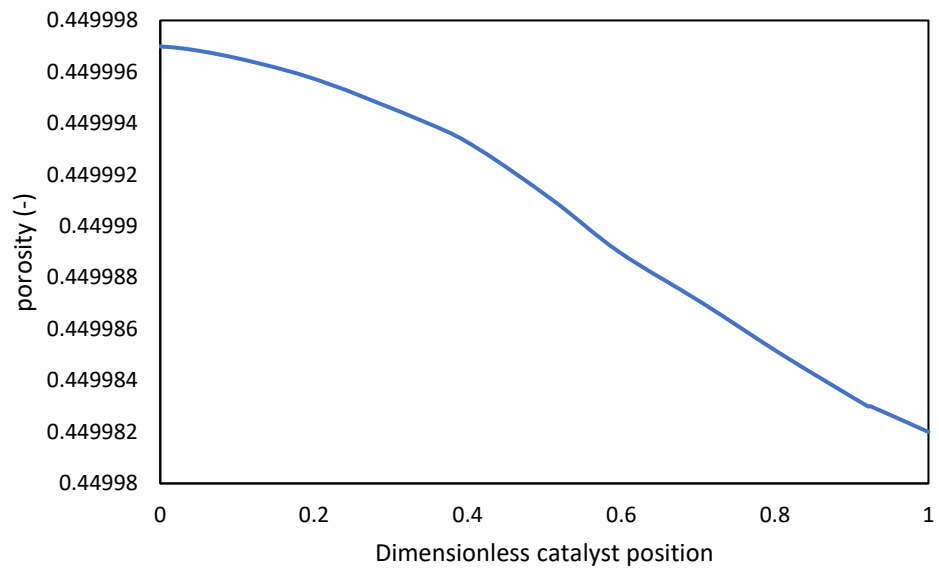


Figure 33 Radius distribution of porosity on the catalyst particle for DRM at 20 sec.

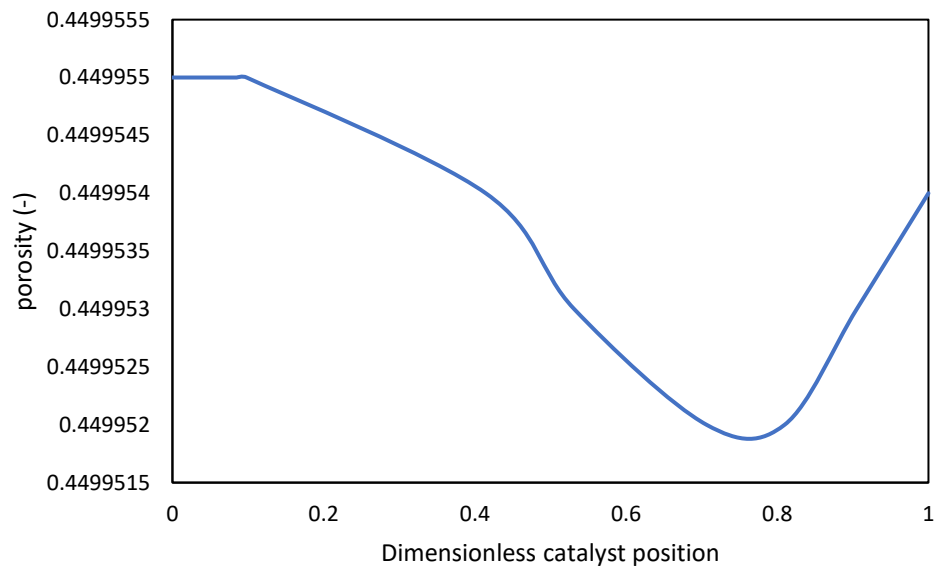


Figure 34 Radius distribution of porosity on the catalyst particle for DRM at 2000 sec.

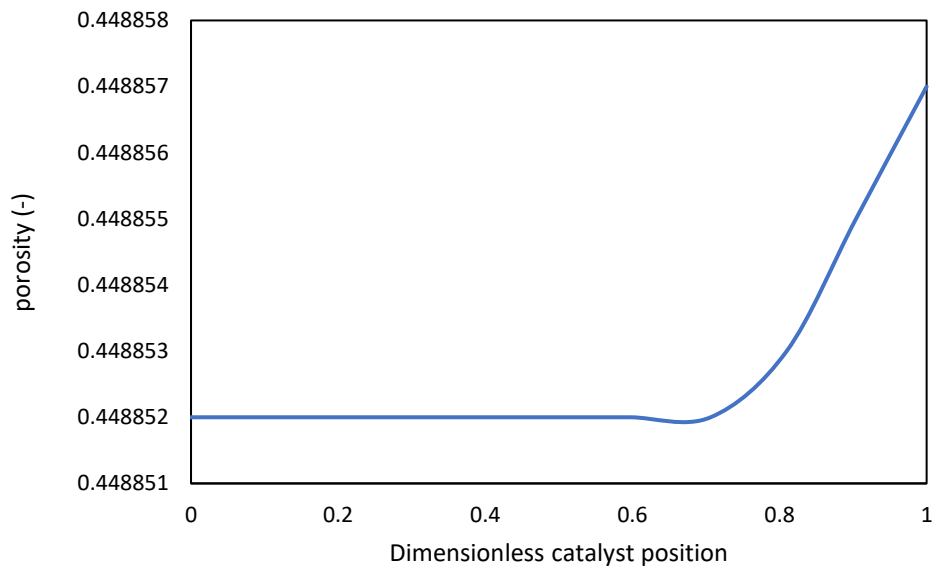


Figure 35 Radius distribution of porosity on the catalyst particle for DRM at 10000 sec

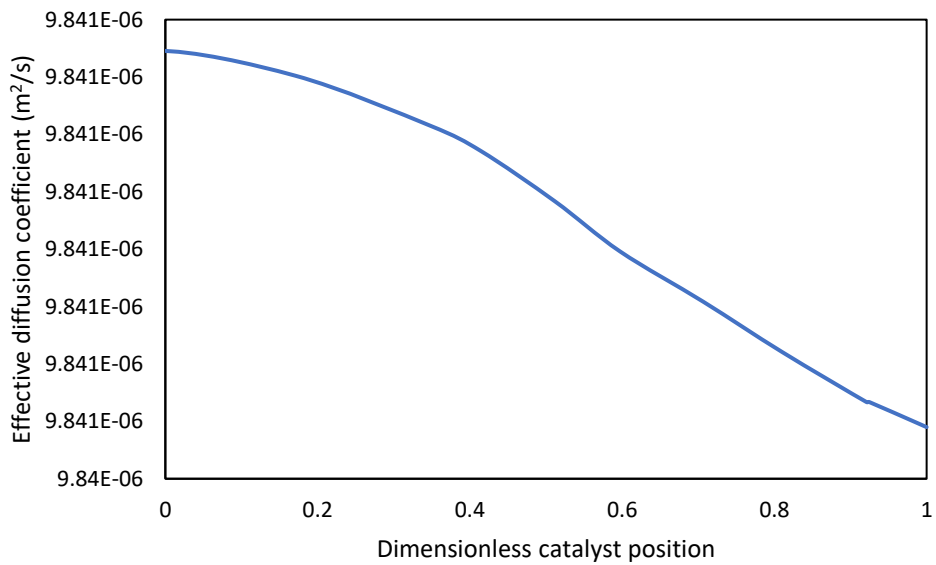


Figure 36 Radius distribution of effective diffusion coefficient on the catalyst particle for DRM at 20 sec.

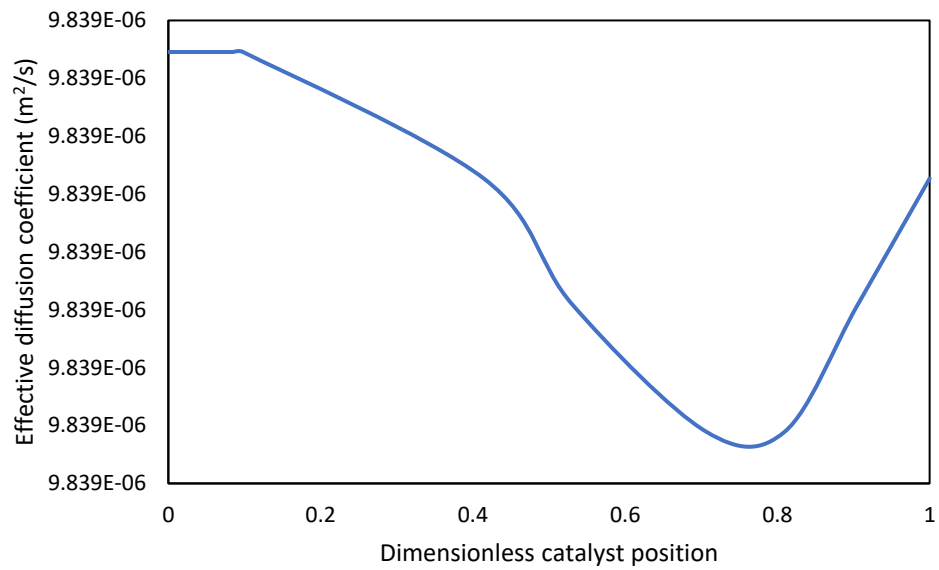


Figure 37 Radius distribution of effective diffusion coefficient on the catalyst particle for DRM at 2000 sec.

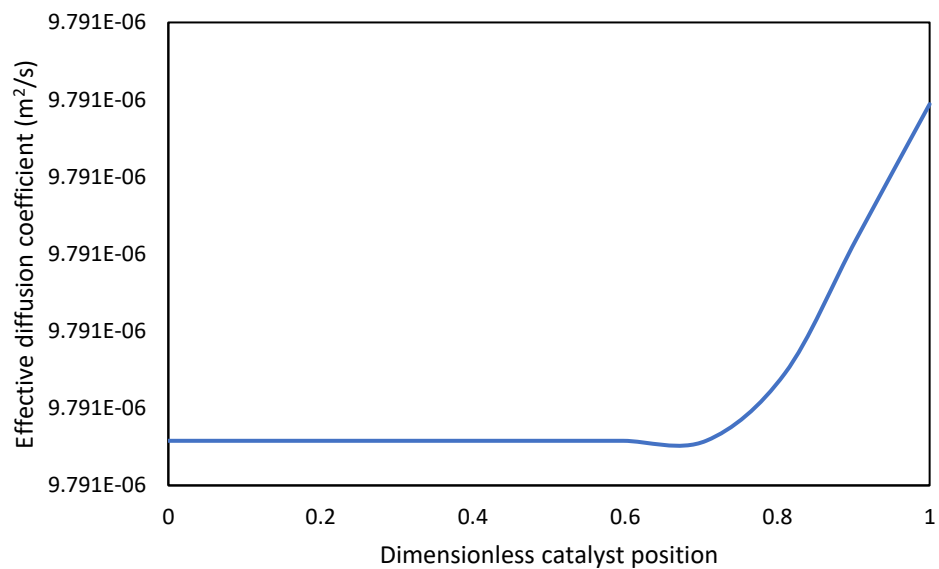


Figure 38 Radius distribution of effective diffusion coefficient on the catalyst particle for DRM at 10000 sec.

4.3.1.4 Temperature

The instantaneous contours of the temperature inside the particle are displayed in Fig. 39. Fig. 40-42 show the radius distribution of temperature inside the catalyst particle at the different reaction times. It can be observed that catalyst surface temperature remains constant at 500 °C by setting the boundary condition. A non-uniform distribution of temperature inside the particle can be observed that a low temperature occurs at the center, which indicates that the heat is transferred from the surface to the center. Moreover, the temperature inside the catalyst particle is below the surface temperature as a result of the nature of the endothermic reaction for the DRM process.



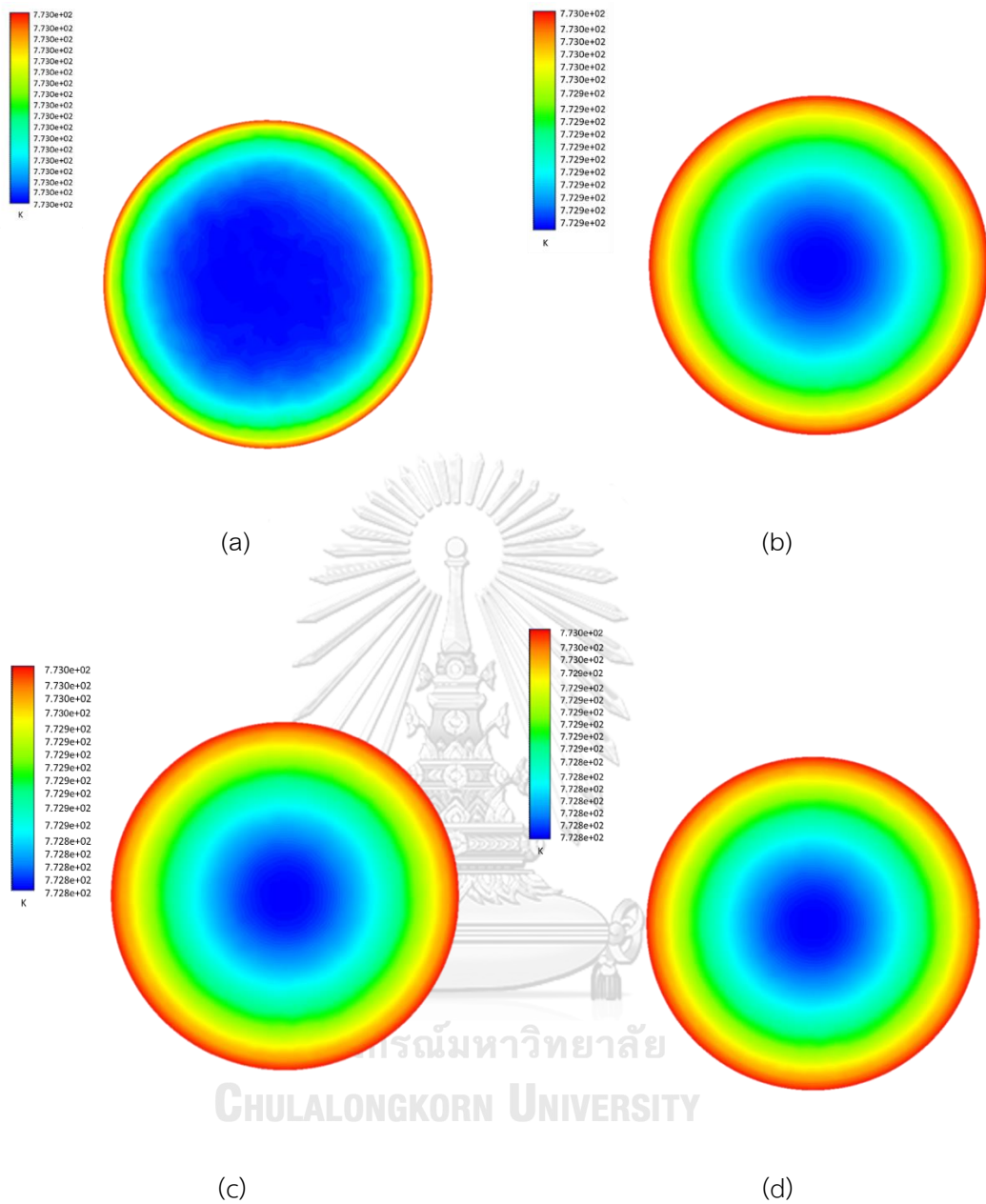


Figure 39 The instantaneous contour of temperature inside the particle at (a) 20 sec (b) 2000 sec (c) 10000 sec (d) 50000 sec.

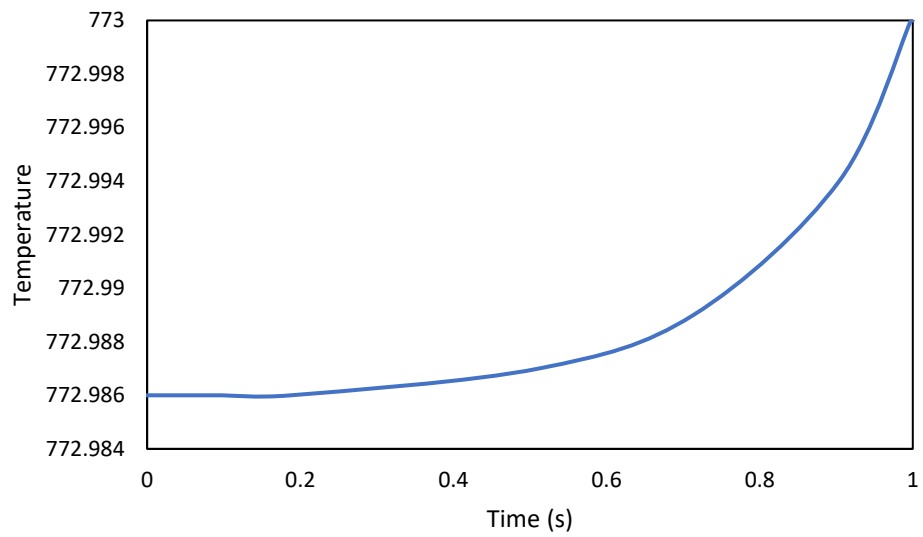


Figure 40 Radius distribution of temperature on the catalyst particle for DRM at 20 sec.

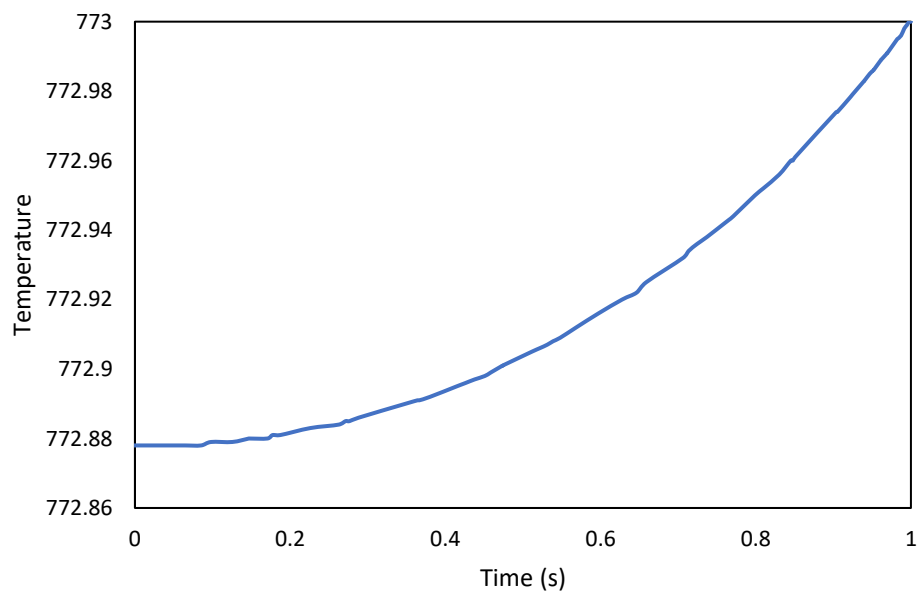


Figure 41 Radius distribution of temperature on the catalyst particle for DRM at 2000 sec.

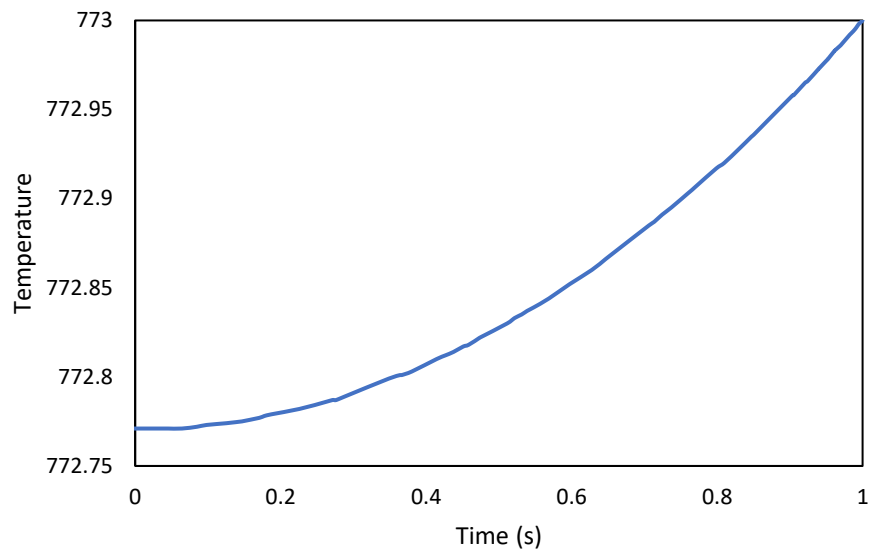


Figure 42 Radius distribution of temperature on the catalyst particle for DRM at 10000 sec.

4.3.2 Effect of operating parameters on coke formation and concentration profile for the DRM reaction

4.3.2.1 CH_4/CO_2 molar ratio

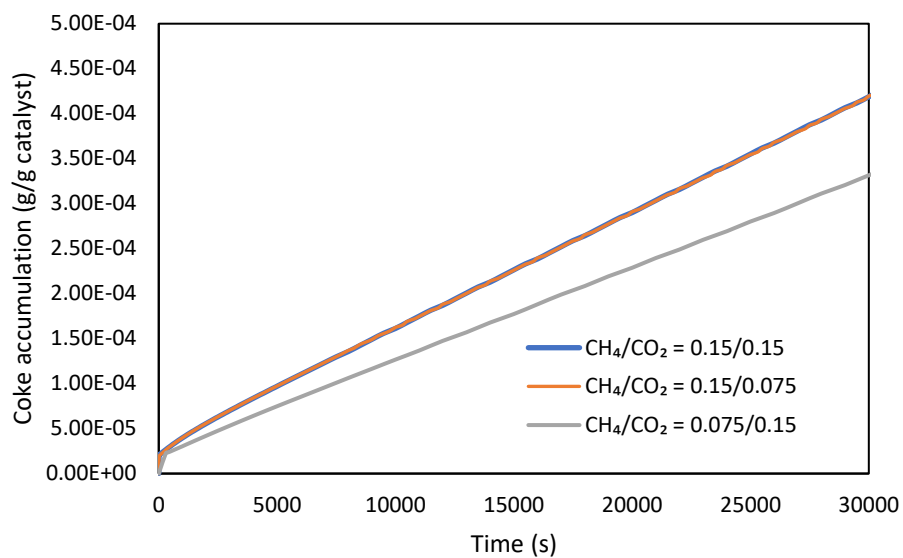


Figure 43 Time dependencies of coke accumulation on the catalyst particle for DRM with different CH₄/CO₂ molar ratios.

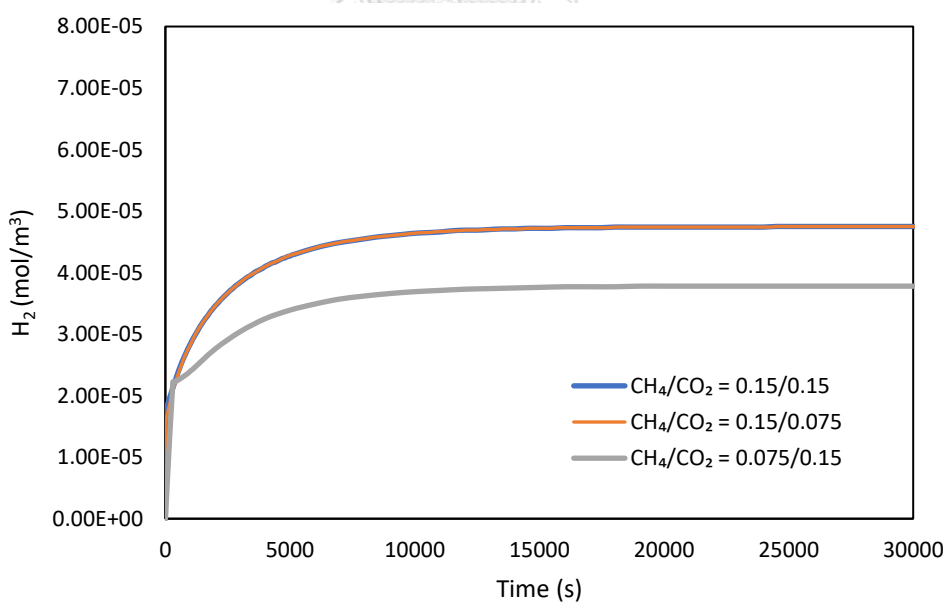


Figure 44 Time dependencies of H₂ concentration on the catalyst particle for DRM with different CH₄/CO₂ molar ratios.

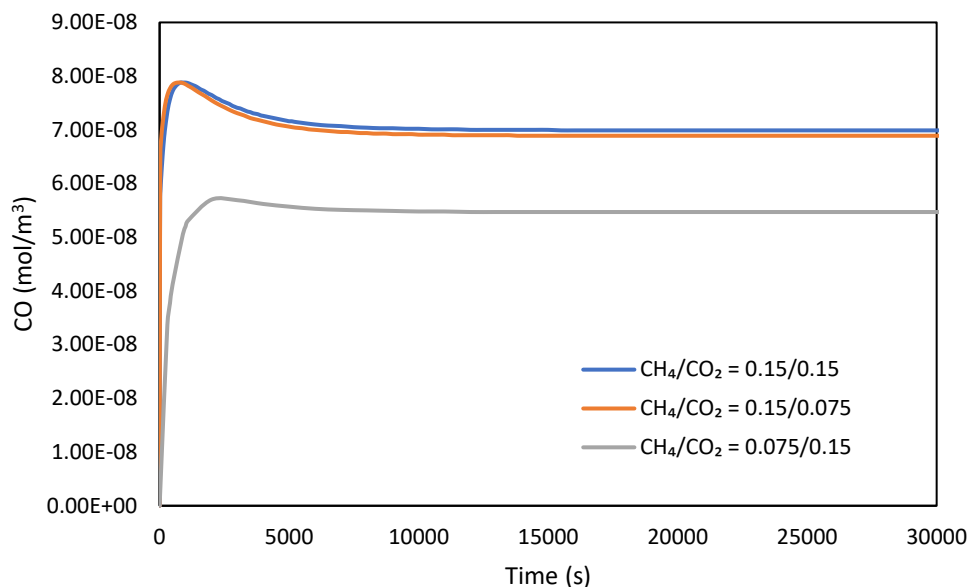


Figure 45 Time dependencies of CO concentration on the catalyst particle for DRM with different CH_4/CO_2 molar ratios.

The effect of the CH_4/CO_2 feed ratio on coke formation was studied at the temperature of 500 °C. The CH_4/CO_2 ratio was performed with the feed composition of 0.15/0.15, 0.15/0.075, and 0.075/0.15. The effect of CH_4 partial pressure was investigated by keeping a constant CO_2 partial pressure, as shown in Fig. 24.

The results show that by increasing CH_4 partial pressure from 0.075 to 0.15 coke formation increase. The H_2 concentration mostly produce from CH_4 decomposition reaction also increase by increasing CH_4 partial pressure which can be seen in Fig. 25. Similarly, the effect of CO_2 partial pressure was investigated by keeping a constant CH_4 partial pressure, as shown in Fig. 24. CO_2 has been found to not affect coke production and H_2 concentration.

Fig. 26 shows CO concentration on the catalyst particle for DRM with different CH_4/CO_2 molar ratios. The results show that increasing CO_2 partial pressure does not affect CO production this is due to the rate expression of DRM in a Langmuir-Hinshelwood used in the simulation reported by Wang et al. (1999) [12]. Wang et al.

(1999) presented that the dependencies of the CO production rate on CH_4 or CO_2 partial pressure, methane showed first order and CO_2 exhibited first order at lower partial pressures (<6 kPa) and zero-order at high pressures.

These results are in agreement with those of Rostrup-Nielsen et al. (1993) [25]. They reported a zero-order dependence in CO_2 partial pressure, as well as a first-order dependence in CH_4 partial pressure in DRM over Ni/Mg(Al)O catalyst. Olsbye et al. (1997) [26] also reported similar results for a Ni/La₂O₃-Al₂O₃ catalyst in DRM at temperatures of 700 to 900 °C. Takano et al. (1994) [27] found similar results over Ni/Al₂O₃ for this reaction. For CO_2 partial pressure lower than 8.4 kPa, the reaction order with respect to CO_2 partial pressure is almost unity, and for CO_2 pressure in the range of 8.4-67.6 kPa, the order is zero.

4.3.2.2 Temperature

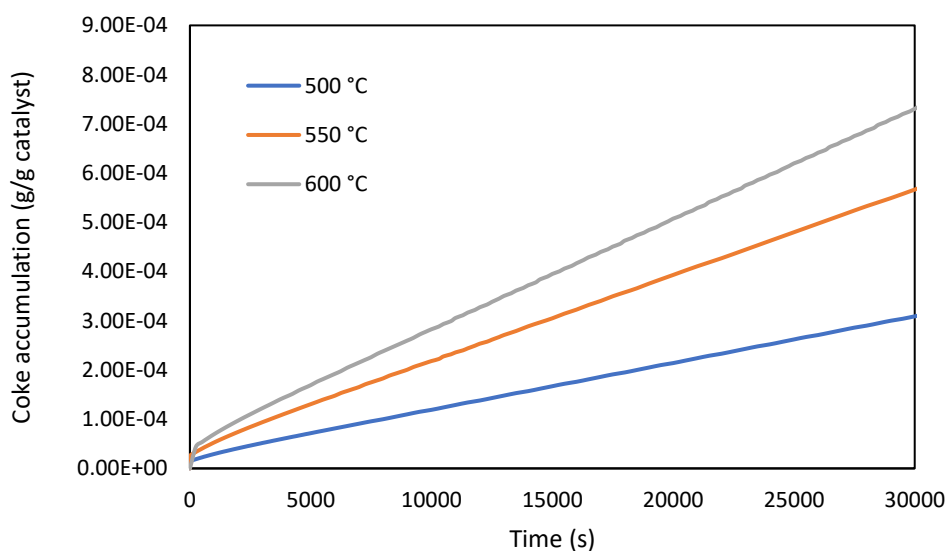


Figure 46 Time dependencies of coke accumulation on the catalyst particle for DRM with different temperatures.

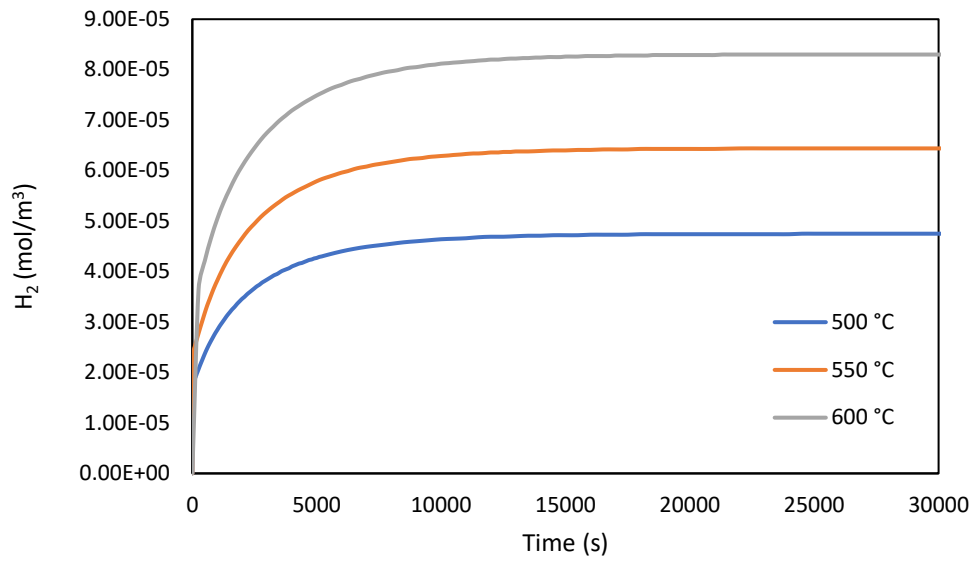


Figure 47 Time dependencies of H₂ concentration on the catalyst particle for DRM with different temperatures.

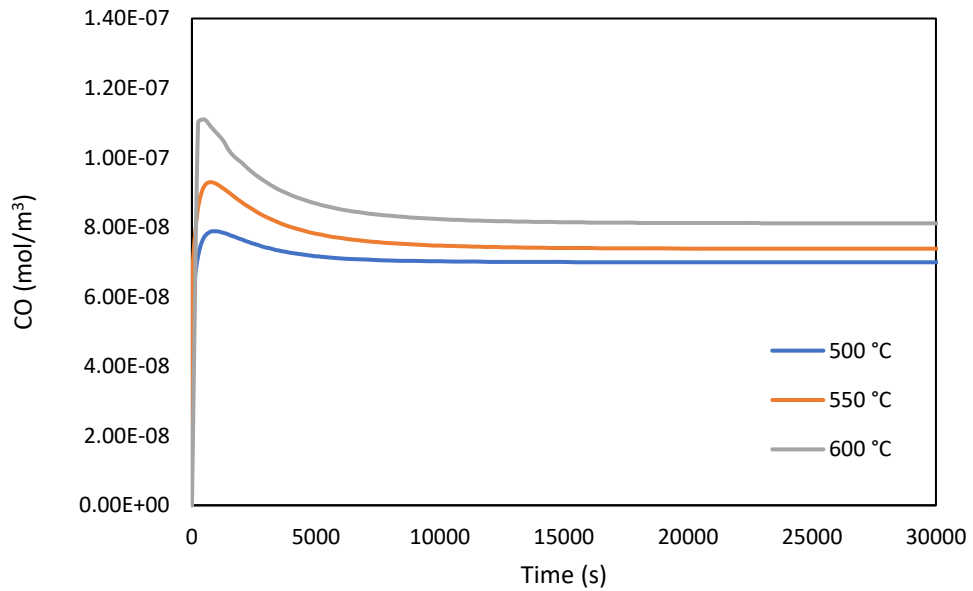
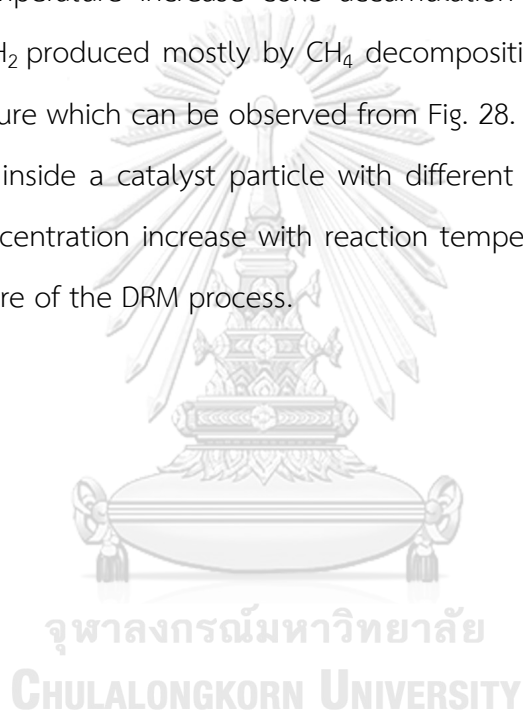


Figure 48 Time dependencies of CO concentration on the catalyst particle for DRM with different temperatures.

The effect of temperature, evaluated in the range of 500 °C to 600 °C, on coke formation was studied in the CH₄/CO₂ ratio of 0.15/0.15. Fig.27 shows coke accumulation inside a single particle of Ni/Al₂O₃ catalyst at different temperatures. When the values of coke accumulation on a catalyst particle at 30000 seconds are compared, it is revealed that temperature of 600 °C and 500 °C have the highest and lowest coke accumulation values of 7.31×10^{-4} and 3.09×10^{-4} g/g catalyst, respectively, whereas the temperature of 550 °C offers 5.67×10^{-4} g/g catalyst. Thus, increasing the temperature increase coke accumulation on catalyst particle. The concentration of H₂ produced mostly by CH₄ decomposition reaction also increases with the temperature which can be observed from Fig. 28. Furthermore, Fig 29 shows CO concentration inside a catalyst particle with different temperatures. The results show that CO concentration increase with reaction temperatures, which reflects the endothermic feature of the DRM process.



CHAPTER V

CONCLUSIONS AND RECOMMENDATIONS

In this research, the catalyst deactivation caused by coke formation over a single particle of Ni/Al₂O₃ catalyst for the DRM process was investigated using computational fluid dynamics (CFD). The results can be concluded as follows:

5.1 Conclusions

- 1 The grid independence test shows that mesh with 222,953 elements provides an accurate result for the values of specific coke accumulation with the maximum relative error of 4 percent compared to mesh with 290,965 elements. Therefore, the grid number of 222,953 with the maximum element size of 0.045 mm is chosen for the simulation.
- 2 The model validation results using the methane decomposition reaction were in good agreement with the experimental data reported by Yang et al. (2021), and the difference between the maximum coke content from simulation and yang et al. results is not more than 5 percent. The comparison of data points is well approximated and fitted the same curve which is obtained from the simulation results.
- 3 The model validation results using coke formation and porosity relation the same trend with the experimental data reported by Zavarukhin et al. Therefore, the model can be used to predict the coke formation in the DRM process.
- 4 The model was optimized and adjusted by using the coke density of 2.36 kg/m³ and particle pore size 15 nm were used in the further simulation for the prediction of coke formation behaviors inside catalyst for DRM process.

- 5 For DRM reaction, the coke was initially formed at the surface of the catalyst and gradually formed at the center. As the reaction progressed, the concentration of coke at the center was higher than at the surface.
- 6 The coke formation inside a catalyst particle has an impact on the porosity and effective diffusion inside the catalyst. The porosity and effective diffusion inside the catalyst are reverse the profiles of coke accumulation.
- 7 The temperature distribution inside the catalyst particle shows a low temperature at the center, which indicates that the heat is transferred from the surface to the center.
- 8 The effect of $\text{CH}_4 / \text{CO}_2$ feed ratio on coke formation shows that increasing the CH_4 partial pressure coke accumulation in the catalyst increased, while CO_2 partial pressure does not affect coke production.
- 9 The effect of temperature on coke formation shows that the increase in temperature raises both coke accumulation and CO concentration in the catalyst due to the endothermic nature of CH_4 decomposition and DRM reaction.

5.2 Recommendations

- 1 Further study to develop the mathematical model for coke formation for DRM by including CO decomposition reaction and reverse water gas shift reaction to make the model be more realistic.
- 2 Further study for the effect of particle shape (i.e. cylinder and hollow cylinder) should be investigated in order to acquire the optimal catalyst shape for the DRM process
- 3 Further study the coke formation in a packed bed model for DRM in order to be used in large-scale production.
- 4 Further study to develop the mathematical model for coke formation for steam and combined steam reforming of methane process.

REFERENCES

1. Song, C., *Global challenges and strategies for control, conversion and utilization of CO₂ for sustainable development involving energy, catalysis, adsorption and chemical processing*. Catalysis today, 2006. **115**(1-4): p. 2-32.
2. Alves, H.J., et al., *Overview of hydrogen production technologies from biogas and the applications in fuel cells*. international journal of hydrogen energy, 2013. **38**(13): p. 5215-5225.
3. Al-Fatesh, A.J.J.o.K.S.U.-E.S., *Suppression of carbon formation in CH₄-CO₂ reforming by addition of Sr into bimetallic Ni-Co/ γ -Al₂O₃ catalyst*. 2015. **27**(1): p. 101-107.
4. Al-Fatesh, A., *Suppression of carbon formation in CH₄-CO₂ reforming by addition of Sr into bimetallic Ni-Co/ γ -Al₂O₃ catalyst*. Journal of King Saud University-Engineering Sciences, 2015. **27**(1): p. 101-107.
5. Hou, Z., et al., *Production of synthesis gas via methane reforming with CO₂ on noble metals and small amount of noble-(Rh-) promoted Ni catalysts*. 2006. **31**(5): p. 555-561.
6. Hou, Z., et al., *Production of synthesis gas via methane reforming with CO₂ on noble metals and small amount of noble-(Rh-) promoted Ni catalysts*. International journal of hydrogen energy, 2006. **31**(5): p. 555-561.
7. Karthik, G. and V.V. Buwa, *A computational approach for the selection of optimal catalyst shape for solid-catalysed gas-phase reactions*. Reaction Chemistry & Engineering, 2020. **5**(1): p. 163-182.
8. Jurković, D.L., et al., *Methane Dry Reforming over Ni/Al₂O₃ Catalyst in Spark Plasma Reactor: Linking Computational Fluid Dynamics (CFD) with Reaction Kinetic Modelling*. Catalysis Today, 2020. **362**: p. 11-21.
9. Lee, S. and H. Lim, *The effect of changing the number of membranes in methane carbon dioxide reforming: A CFD study*. Journal of Industrial and Engineering Chemistry, 2020. **87**: p. 110-119.
10. Zhang, H., et al., *Thermal-chemical reaction characteristics of Ni/Al₂O₃*

- catalytic porous material filled solar reactor for dry reforming of methane process.* Applied Thermal Engineering, 2020. **180**: p. 115901.
11. Borisova, E. and P. Adler, *Deposition in porous media and clogging on the field scale.* Physical Review E, 2005. **71**(1): p. 016311.
 12. Wang, S. and G. Lu*, *A comprehensive study on carbon dioxide reforming of methane over Ni/Y-Al₂O₃ catalysts.* Industrial & engineering chemistry research, 1999. **38**(7): p. 2615-2625.
 13. Zavarukhin, S.G. and G.G. Kuvshinov, *The kinetic model of formation of nanofibrous carbon from CH₄-H₂ mixture over a high-loaded nickel catalyst with consideration for the catalyst deactivation.* Applied Catalysis A: General, 2004. **272**(1-2): p. 219-227.
 14. Yang, X., et al., *Evaluation of coke deposition in catalyst particles using particle-resolved CFD model.* Chemical Engineering Science, 2021. **229**: p. 116122.
 15. Snoeck, J.-W., G. Froment, and M. Fowles, *Kinetic study of the carbon filament formation by methane cracking on a nickel catalyst.* Journal of Catalysis, 1997. **169**(1): p. 250-262.
 16. Wehinger, G.D., T. Eppinger, and M. Kraume, *Evaluating catalytic fixed-bed reactors for dry reforming of methane with detailed CFD.* Chemie Ingenieur Technik, 2015. **87**(6): p. 734-745.
 17. Froment, G.F., K.B. Bischoff, and J. De Wilde, *Chemical reactor analysis and design.* Vol. 2. 1990: Wiley New York.
 18. Snoeck, J.-W., G. Froment, and M. Fowles, *Kinetic Evaluation of Carbon Formation in Steam/CO₂-Natural Gas Reformers. Influence of the Catalyst Activity and Alkalinity.* International Journal of Chemical Reactor Engineering, 2002. **1**(1).
 19. Beeckman, J.W. and G.F. Froment, *Deactivation of catalysts by coke formation in the presence of internal diffusional limitation.* Industrial & Engineering Chemistry Fundamentals, 1982. **21**(3): p. 243-250.
 20. Argyle, M.D. and C.H. Bartholomew, *Heterogeneous catalyst deactivation and*

- regeneration: a review*. Catalysts, 2015. **5**(1): p. 145-269.
21. Gao, X., et al., *Anti-coking and anti-sintering Ni/Al₂O₃ catalysts in the dry reforming of methane: recent progress and prospects*. Catalysts, 2021. **11**(8): p. 1003.
 22. Yang, X., et al., *Investigation of coke deposition inside catalyst with heterogeneous active component distribution*. Fuel, 2021. **287**: p. 119547.
 23. Wang, S. and G.M. Lu, *Reaction kinetics and deactivation of Ni-based catalysts in CO₂ reforming of methane*, in *Reaction engineering for pollution prevention*. 2000, Elsevier. p. 75-84.
 24. Voorhies Jr, A., *Carbon formation in catalytic cracking*. Industrial & Engineering Chemistry, 1945. **37**(4): p. 318-322.
 25. Rostrupnielsen, J. and J.B. Hansen, *CO₂-reforming of methane over transition metals*. Journal of Catalysis, 1993. **144**(1): p. 38-49.
 26. Olsbye, U., T. Wurzel, and L. Mleczko, *Kinetic and reaction engineering studies of dry reforming of methane over a Ni/La/Al₂O₃ catalyst*. Industrial & engineering chemistry research, 1997. **36**(12): p. 5180-5188.
 27. Takano, A., T. Tagawa, and S. Goto, *Carbon dioxide reforming of methane on supported nickel catalysts*. Journal of chemical engineering of Japan, 1994. **27**(6): p. 727-731.



จุฬาลงกรณ์มหาวิทยาลัย
CHULALONGKORN UNIVERSITY

VITA

NAME Chananun Rojanarungruengporn

DATE OF BIRTH 20 December 1996

PLACE OF BIRTH Bangkok

INSTITUTIONS ATTENDED Graduated in bachelor's degree from Faculty of Science in Chemical Technology, Chulalongkorn University in 2019.

HOME ADDRESS Sao Thong Hin, Bang Yai, Nonthaburi 11140

